The Astrophysical Journal, 929:107 (19pp), 2022 April 10 https://doi.org/10.3847/1538-4357/ac5910

Iron-60 in the Early Solar System Revisited: Insights from In Situ Isotope Analysis of Chondritic Troilite

János Kodolányi[1], Peter Hoppe[1], Christian Vollmer[2], Jasper Berndt[2], and Maren Müller[3]
[1] Max Planck Institute for Chemistry, Hahn-Meitner-Weg 1, D-55128 Mainz, Germany; j.kodolanyi@mpic.de
[2] University of Münster, Institute for Mineralogy, Corrensstrasse 24, D-48149 Münster, Germany
[3] Max Planck Institute for Polymer Research, Ackermannweg 10, D-55128 Mainz, Germany
Received 2022 January 20; revised 2022 February 25; accepted 2022 February 26; published 2022 April 18

Abstract

We measured the nickel isotope composition of troilites from chondritic meteorites using the NanoSIMS to put constraints on the abundance of iron-60 in the early solar system. The troilites were selected from petrologic type 3 ordinary and carbonaceous chondrites. Based on petrographic observations and mineral chemistry, the troilites targeted for isotope analysis crystallized from melts, most likely in a nebular setting. Our isotope analyses did not reveal any significant correlation between nickel-60 enrichments and Fe/Ni ratios, either in the entire set of troilite grains or in individual troilites. The average inferred initial $^{60}Fe/^{56}Fe$ ratio of the studied troilites (i.e., the $^{60}Fe/^{56}Fe$ ratio calculated for the entire troilite population) is 1.05 ($\pm$1.48) $\times 10^{-8}$. This value is very similar to those estimated in the past for Semarkona chondrules, angrites, as well as diogenites and eucrites, based on the isotope analyses of bulk samples (10^{-9}–10^{-8}), but about two orders of magnitude smaller than the average initial $^{60}Fe/^{56}Fe$ ratios inferred previously for Semarkona troilites and many chondrules from ordinary and carbonaceous chondrites (10^{-7}–10^{-6}) using in situ analysis techniques. Based on petrographic evidence, and the generally unequilibrated nature of our samples, as well as on the timing of chondrule formation and planetary evolution, the lack of discernible signs of in situ iron-60 decay in the studied troilites is probably unrelated to metamorphic re-equilibration, and it is also not the result of a late formation of the troilites. We suggest that the highest inferred initial $^{60}Fe/^{56}Fe$ ratios reported in the literature are probably inaccurate.

1. Introduction

Iron-60 is a short-lived radioactive isotope with a half-life ($t_{\frac{1}{2}}$) of 2.62 $\pm$ 0.04 million years (Rugel et al. 2009; Wallner et al. 2015; Ostdiek et al. 2017; throughout this paper, all quoted uncertainties represent the 68% confidence level, abbreviated as $\pm 1\sigma$, unless stated otherwise). It is formed in neutron-rich stellar environments (neutron density $\gtrsim 3 \times 10^{10} \times cm^{-3}$; Limongi & Chieffi 2006), so the most important stellar sources of iron-60 in the Milky Way are intermediate-mass and massive stars (Wasserburg et al. 2006). Upon β^- decay, iron-60 turns into cobalt-60, which forms stable nickel-60 through another β^- decay ($t_{\frac{1}{2}}(^{60}Co) = 5.2712 \pm 0.0004$ yr; Browne & Tuli 2013).

Given the nucleosynthetic conditions conducive to its formation, iron-60 was recognized early on as one of the short-lived radioactive isotopes whose abundance in the early solar system is key to constraining the sources of solar system matter (Birck & Lugmair 1988). In general, a higher abundance of iron-60 could indicate a larger time-integrated contribution of intermediate-mass and massive stars to the protosolar dust and gas cloud, and the types of those massive stellar sources and the timing of iron-60 addition can be constrained from the presence or absence of collateral isotope effects (e.g., Vescovi et al. 2018). The potential role of iron-60 in the thermal evolution of early planetary bodies has also been recognized a long time ago (Shukolyukov & Lugmair 1993). The decay of iron-60 and cobalt-60 produces heat (2.712 MeV per ^{60}Fe; Castillo-Rogez et al. 2009), which, depending on the original abundance of iron-60, could influence the thermal structure of early solar system planetesimals (e.g., Sahijpal et al. 2007). Despite its importance, however, the abundance of iron-60 in the early solar system has been the subject of considerable debate. This debate contributed to the shifts in our view on the stellar sources of short-lived radioactive isotopes in the early solar system and on the role of iron-60, besides radioactive aluminum-26 ($t_{\frac{1}{2}} = 705{,}000$ yr; Norris et al. 1983), as a heat source in planetary differentiation (e.g., Dwarkadas et al. 2017; Neumann et al. 2018). Because of its longer half-life, iron-60 would have kept planetesimals thermally active for a much longer time than aluminum-26 alone (Moskovitz & Gaidos 2011; Yoshino et al. 2003), provided it was present in sufficient quantities.

At the core of the aforementioned debate is the difference between the inferred initial $^{60}Fe/^{56}Fe$ ratios of early solar system objects estimated from in situ analyses and from the analyses of bulk samples. In particular, in situ analyses of several chondrules and troilite grains indicated a one to two orders of magnitude higher $^{60}Fe/^{56}Fe$ ratio in the early solar system at the time the so-called canonical calcium-aluminum-rich inclusions (CCAIs; see Jacobsen et al. 2008) formed than data obtained from the analysis of all but a few bulk samples (see Figure 1 and the review of existing data below). The highest $^{60}Fe/^{56}Fe_{CCAI}$ ratio, $13.1 \pm 2.3 \times 10^{-7}$, was estimated by Mishra & Goswami (2014), based on in situ iron–nickel and aluminum–magnesium isotope data from SIMS (secondary ion mass spectrometry) measurements of a chondrule in the unequilibrated ordinary chondrite (UOC) Semarkona (Figure 1). Similarly high initial $^{60}Fe/^{56}Fe_{CCAI}$ ratios (or $^{60}Fe/^{56}Fe$ ratios, if age data are not available) have been inferred for several other chondrules (e.g., Mishra et al. 2016; Telus et al. 2018) and troilite grains (Mostefaoui et al. 2005). In contrast, all inferred $^{60}Fe/^{56}Fe_{CCAI}$ ratios estimated from isotope data obtained on bulk samples until

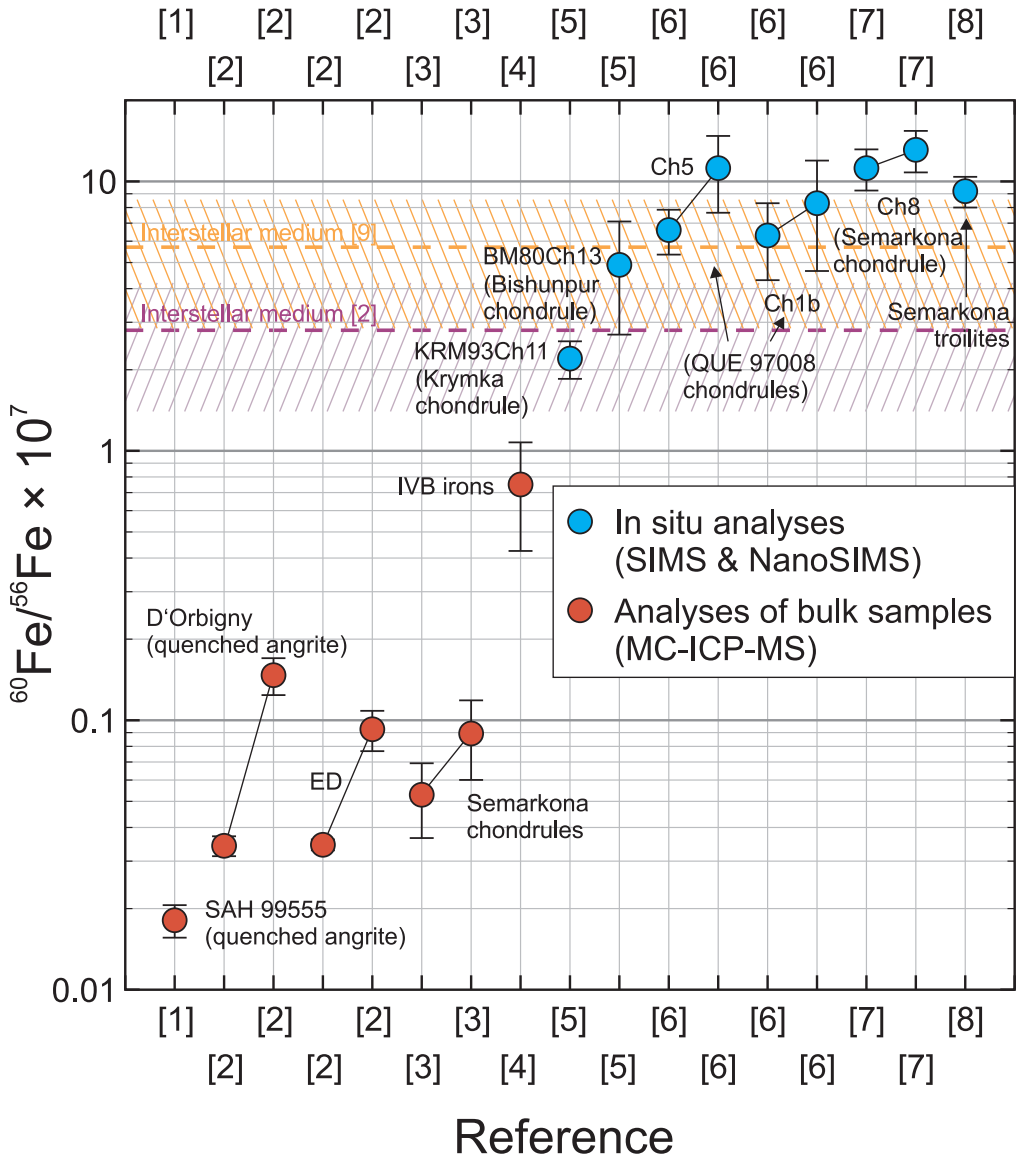

Figure 1. Inferred initial ^{60}Fe/^{56}Fe ratios of solar system objects. The names and nature of the objects are indicated close to the data points. Note that not all inferred ^{60}Fe/^{56}Fe ratios reported in the literature are displayed. The depicted selection of ratios, however, is representative of the maxima estimated for different kinds of objects and analytical techniques. Tie lines connect the ^{60}Fe/^{56}Fe ratio inferred for a sample at its formation with the ratio that was calculated for the solar system from the same sample using its age, for the time CCAIs formed. Uncertainties correspond to $\pm 1\sigma$. Abbreviations: SIMS = secondary ion mass spectrometry, MC-ICP-MS = multicollector inductively coupled plasma mass spectrometry, ED = meteorites belonging to the eucrite or diogenite groups. "Interstellar medium" refers to the average ^{60}Fe/^{56}Fe ratio of the interstellar medium of the Milky Way at the time of solar system formation (hatch-patterned areas represent uncertainties quoted by the literature sources). References: [1] = Quitté et al. (2010), [2] = Tang & Dauphas (2012), [3] Tang & Dauphas (2015), [4] Steele et al. (2012)], [5] Telus et al. (2018), [6] Mishra et al. (2016), [7] Mishra & Goswami (2014), [8] Mostefaoui et al. (2005), [9] Diehl et al. (2021).

2021 were below 8×10^{-8}, and, if we disregard the uncertain ^{60}Fe/^{56}Fe estimate of Steele et al. (2012) for IVB iron meteorites, below 1.5×10^{-8} (Figure 1). Only a recent study by Cook et al. (2021), based also on bulk IVB (and IID) iron meteorite data, estimated a much higher ^{60}Fe/^{56}Fe$_{CCAI}$ ratio of $6.4 \pm 1.0 \times 10^{-7}$, which is more in line with the in situ results. Isotopically, the IVB and IID irons belong to the carbonaceous meteorites, whereas all other meteorites with estimated ^{60}Fe/^{56}Fe based on bulk isotope data belong to the noncarbonaceous meteorites (Warren 2011; Nanne et al. 2019), so the higher ^{60}Fe/^{56}Fe ratios inferred for bulk IVB and IID meteorites may indicate iron-60 heterogeneity in the early solar system. Nevertheless, the ^{60}Fe/^{56}Fe$_{CCAI}$ ratios inferred by Cook et al. (2021) are probably overestimations. They were calculated based on the nickel-60 deficit in IVB and IID meteorites, which have subchondritic Fe/Ni ratios, relative to CI chondrites, which have chondritic Fe/Ni ratios. The authors assumed that the IID and IVB precursors evolved with a chondritic Fe/Ni ratio until core formation in their parent bodies. CI chondrites have terrestrial, whereas all other carbonaceous chondrites have subterrestrial, ^{60}Ni/^{58}Ni ratios despite having about the same Fe/Ni ratios, and there are carbonaceous chondrites that show more similarity in their ^{62}Ni/^{58}Ni and ^{64}Ni/^{58}Ni ratios to the IVB and IID irons than does the CI group (Steele et al. 2012; Nanne et al. 2019). Thus, a different basis of comparison of the IVB and IID data of Cook et al. (2021) would drastically reduce the calculated ^{60}Fe/^{56}Fe$_{CCAI}$ ratios (by more than a factor of 4), and it could be better justified, too. All in all, the main body of available nickel isotope data on bulk meteoritic samples points to at least one order of magnitude lower ^{60}Fe/^{56}Fe$_{CCAI}$ than data obtained

in situ. Importantly, chondrules from Semarkona were studied using both bulk and in situ techniques, and whereas initial $^{60}Fe/^{56}Fe$ ratios exceeding 10^{-7} by more than expected from quoted uncertainties at the 95% confidence level (by $>2\sigma$) were estimated for several chondrules based on SIMS data (Mishra & Goswami 2014; Mishra & Chaussidon 2014), the analyses of bulk chondrules gave a completely different picture (Tang & Dauphas 2015). Only one individual chondrule had a significant ($>2\sigma$) nickel-60 enrichment (SC-13-6), and even for this chondrule, an initial $^{60}Fe/^{56}Fe$ ratio of only $3.38 \pm 1.44 \times 10^{-9}$ can be estimated. It should be noted that the in situ measurement of a chondrule from Semarkona by resonance ionization mass spectrometry yielded an inferred $^{60}Fe/^{56}Fe$ ratio of $3.8 \pm 3.5 \times 10^{-8}$ (Trappitsch et al. 2018), compatible with the data of bulk samples.

There are several, mutually not exclusive, potential explanations for the discrepancy in inferred initial $^{60}Fe/^{56}Fe$ ratios from studies that rely on in situ and bulk analyses. For example, initial $^{60}Fe/^{56}Fe$ ratios estimated from bulk samples may be biased if certain minerals are preferentially removed during sample rinsing to get rid of contamination. Quitté et al. (2011) observed that even a few minutes of rinsing of the Bouvante eucrite with acetone removed tens of percent of the sample's nickel, and that the residue had a higher Fe/Ni ratio than the wash solution. They also observed that different mineral fractions of the Juvinas eucrite did not lie on the bulk rock iron–nickel isochron (i.e., that the iron–nickel system was disturbed). As it is common to use stronger agents than acetone, such as HCl, to remove contamination from bulk samples (e.g., Tang & Dauphas 2012), there is a possibility of getting biased isotopic compositions and Fe/Ni ratios for bulk samples. Nevertheless, it is unlikely that the disturbance of the iron–nickel system and sample rinsing can explain the bulk–in situ duality of inferred $^{60}Fe/^{56}Fe$ ratios. There are several samples in the bulk rock data record with no sign of significant disturbance of the iron–nickel system, and low inferred $^{60}Fe/^{56}Fe$ (and $^{60}Fe/^{56}Fe_{CCAI}$) ratios. For example, Tang & Dauphas (2012) calculated an initial $^{60}Fe/^{56}Fe$ ratio of $3.42 \pm 0.58 \times 10^{-9}$ and an $^{60}Fe/^{56}Fe_{CCAI}$ of $1.47 \pm 0.46 \times 10^{-8}$ for the quenched angrite d'Orbigny, based on an internal mineral isochron, with an initial $\varepsilon^{60}Ni$ of 0.00 ± 0.06 ($\varepsilon^{60}Ni = [(^{60}Ni/^{58}Ni)_{sample})/(^{60}Ni/^{58}Ni)^{-1}_{SRM986}] \times 10,000$; SRM986 is a reference material distributed by the National Institute of Standards and Technology).

In situ data can also be biased. For example, a large number of early in situ data are biased because of an error in data reduction, wherein some authors used the averages of isotope ratio measurements to obtain the isotope ratio of a single spot. This error affected data not only for the iron–nickel system but also for other short-lived radioactive systems (see Telus et al. 2012, who also provided a recalculation of some of the earlier biased results). Telus et al. (2016) also warned of the effects of iron–nickel redistribution in chondrules by aqueous alteration after the decay of iron-60. They argued that cracks, often only a few microns across, filled with iron- and/or iron- and nickel-rich minerals could not be avoided completely during SIMS analyses, let alone during the analyses of bulk chondrules, and that inclusion of such minerals in the analyzed material might negatively bias calculated initial $^{60}Fe/^{56}Fe$ ratios. However, the observations of Telus et al. (2016) on iron–nickel mobility in chondrules cannot be applied to many differentiated rocks from the early solar system that were studied by bulk analytical methods (angrites and eucrites; e.g., Tang & Dauphas 2012, 2015). Elliott & Steele (2017) suggested that some of the in situ measurements might have suffered from the effect of $^{59}Co^{1}H$ interference on mass 60. Although their models relied heavily on the ill-constrained Co/Ni ratios of chondrule minerals, they highlighted the importance of the proper treatment of isobaric interferences during in situ analyses.

Early on, chondritic troilite (ideal formula: FeS) became a target of in situ isotope measurements for the estimation of initial $^{60}Fe/^{56}Fe$ ratios, because of its variable, but often low, native nickel content (Fe/Ni ratios up to ~230,000; Tachibana & Huss 2003; Mostefaoui et al. 2005). However, the interpretation of chondritic troilite data is complicated by the fact that troilite can have different origins (nebular processes, thermal metamorphism, hydrothermal alteration), as well as by the fact that its age cannot be determined directly, and the focus of in situ studies soon shifted to silicates. Initial $^{60}Fe/^{56}Fe$ ratios estimated for chondritic troilites (from petrologic type 3–3.2 ordinary and enstatite chondrites) based on in situ analyses initially showed considerable variation, from about 10^{-7} to about 2×10^{-6} (Tachibana & Huss 2003; Mostefaoui et al. 2005; Guan et al. 2007). However, most of these in situ troilite data were affected by an error in data reduction (averaging of measured ratios; see the previous paragraph) that introduced positive bias in calculated initial $^{60}Fe/^{56}Fe$ ratios (Tachibana & Huss 2003; Guan et al. 2007; see discussion by Telus et al. 2012). After correction of the biased data, Telus et al. (2012) found that neither the data of Tachibana & Huss (2003) nor those of Guan et al. (2007) showed evidence for in situ iron-60 decay at the 95% confidence level. The data set of Mostefaoui et al. (2005) did not suffer from the above-mentioned bias, and remains until today the only set of in situ data on chondritic troilite that indicates in situ iron-60 decay at the $\geqslant$95% confidence level, with an $^{60}Fe/^{56}Fe$ of $9.2 \pm 1.2 \times 10^{-7}$.

The above in situ troilite measurements were performed by SIMS, using either the IMS-6f or the NanoSIMS (both produced by Cameca). In order to strike an acceptable balance between analytical accuracy, precision, and spatial resolution, these measurements had to be performed with spot sizes (diameters) of $\sim 10\,\mu$m or larger (Figure 2). Since these investigations, however, the spatial resolution of SIMS instruments has improved. This allows spot sizes of only a few microns in diameter (Figure 2; see also Section 3) and the detection of submicron impurities. Thus, a lot, if not all, of the inclusions and veins that potentially influence the measured isotope compositions can be avoided, improving overall accuracy.

Here we present new nickel isotope data and Fe/Ni ratios measured in situ in chondritic troilite grains using NanoSIMS and supplement the isotope data with submicron-scale textural and chemical observations by transmission electron microscopy on electron-transparent slices of selected troilites. Our goal was to follow up on early in situ studies with an improved analytical setup and include troilites from carbonaceous chondrites in order to gain a better understanding of the causes of the variability of estimated initial $^{60}Fe/^{56}Fe$ ratios in the literature.

2. Samples

In order to find troilite grains least affected by metamorphism or aqueous alteration on the parent body, we selected five chondrites of petrologic type ~3 for our study (Semarkona, Queen Alexandra Range 97008, Meteorite Hills 00526,

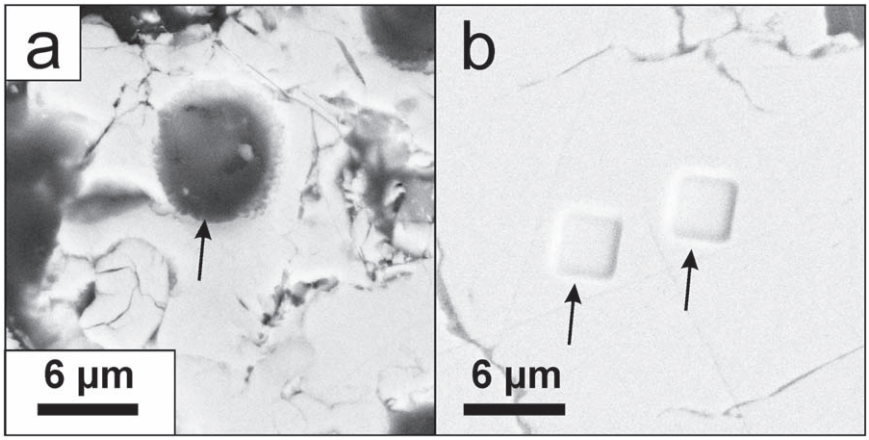

Figure 2. Backscattered electron images of NanoSIMS analysis spots (arrows) in troilite (light gray). (a) Typical pit of the measurements of Mostefaoui et al. (2005) in Semarkona, performed using the Duoplasmatron primary ion source available at the time. (b) Typical 3×3 μm^2 pits of the present study in MET 00526, after O^- bombardment using today's Hyperion primary ion source. Meteorite Hills 00526 L(LL) 3.05 ordinary chondrite. Note that the pit in (a) was probably larger at the time of the measurement because the sample surface has been polished since the study by Mostefaoui et al. (2005).

Dominion Range 08006, and Allan Hills A77307; Table 1). Although these meteorites do show some signs of terrestrial weathering and/or parent-body alteration, based on the chromium content of their ferroan olivines, as well as the presence of amorphous silicates and/or variable amounts of presolar grains in their matrices, they are among the least heated or aqueously altered chondrites known (Grossman & Brearley 2005; Floss & Haenecour 2016; Nittler et al. 2018; Davidson et al. 2019; Dobrică & Brearley 2020). The only exception is Semarkona, which experienced a more pronounced aqueous alteration on its parent body (e.g., Alexander 1989; Dobrică & Brearley 2020). However, Semarkona also happens to be the only meteorite with a clear indication of in situ iron-60 decay in troilite (Mostefaoui et al. 2005). Since the thin section of Semarkona investigated by Mostefaoui et al. (2005) was still available for us, we found it very important to include this meteorite in our study.

Ideally, the primary targets of isotope analysis should be nickel-poor troilite grains with likely high-temperature origin ($T \geqslant$ several hundred kelvin) that predate the formation of the meteorites' parent bodies and cooled rapidly relative to the half-life of iron-60 (i.e., on an orders-of-magnitude shorter timescale). Because the meteorites did not experience thermal metamorphism on their parent bodies, such troilite grains should record the last nebular heating event before their capture. Their $^{60}Ni/^{62}Ni$ ratios would thus be expected to reflect isotopic equilibration during that heating event, and the decay of iron-60 since then, provided aqueous alteration did not alter element and isotope compositions. However, the origin and history of troilite are not always straightforward to establish (see Section 5). In general, troilites that, based on their texture, appeared to be the products of crystallization from a melt and had high Fe/Ni ratios were chosen for isotope analysis.

Table 1
Studied Meteorites

Name	Abbreviation Used in the Text	Group	Petrologic Type
Carbonaceous meteorites			
Dominion Range 08006	DOM 08006	CO	3
Allan Hills A77307	ALHA77307	CO	3.0
Noncarbonaceous meteorites			
Semarkona	⋯	LL	3.00
Queen Alexandra Range 97008	QUE 97008	L	3.05

Note. Meteorite groups and types according to the Meteoritical Bulletin Database (December 2021).

3. Analytical Methods

3.1. Scanning Electron Microscopy and Electron Probe Microanalysis

We used backscattered electron (BSE) images and energy-dispersive X-ray (EDX) element maps to select sulfide grains potentially suitable for isotope analysis. BSE imaging and EDX mapping were carried out on conventional petrographic thin sections with the LEO 1530 field emission scanning electron microscope (SEM) at the Max Planck Institute for Chemistry (Mainz, Germany), equipped with an Oxford X-Max 80 mm^2 energy-dispersive X-ray detector. Point analyses with the same instrument (15 kV acceleration voltage, 90 s measurement time without detector dead time, quantification with Aztec 2.4 and 3.1) were performed on sulfides and associated phases to search for troilites without a discernible nickel peak in the EDX spectrum (which indicates an Fe/Ni ratio of a couple of thousands, or higher) and to quantify the Fe/Ni ratios of nickel-rich sulfides. The major and minor element composition of some of the target sulfide and associated metal grains were also measured using the JEOL JXA 8530F electron microprobe at the University of Münster (UM; Münster, Germany). For these measurements, the acceleration voltage and beam current were 15 kV and 80 nA, respectively. The probe diameter was about 2 μm. Raw data were corrected for matrix effects following the PRZ method (Phi-Rho-Zed, a ZAF correction that uses a Gaussian depth distribution function for the calculation of absorption correction; Armstrong 1991). Quantification was based on a wavelength dispersive X-ray spectrometer–intensity comparison of unknowns with natural and synthetic sulfide and metal reference materials. The detection limit for nickel was about 30 parts per million by weight.

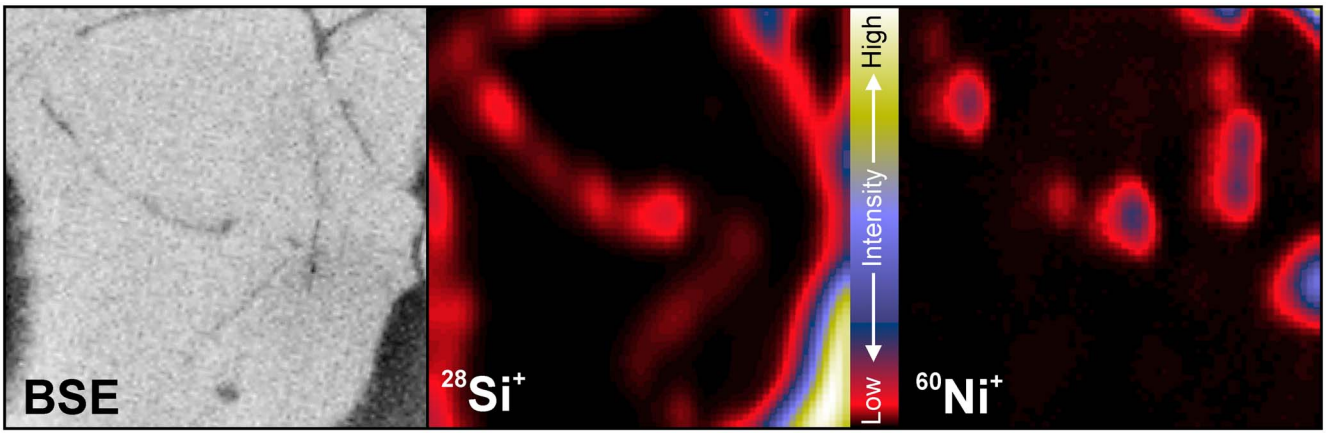

Figure 3. Backscattered electron image (left), and NanoSIMS ion images of a thoroughly fractured troilite in Semarkona (region of interest S5). Individual images correspond to $6 \times 6\ \mu m^2$. The color key is valid for both ion images.

3.2. In Situ Isotope Analysis

Isotope measurements were performed using NanoSIMS 50 of the Max Planck Institute for Chemistry in Mainz, Germany, using the Hyperion primary ion source in O^- mode. The primary ion beam intensity was approximately 75 pA (lens L1 ≈ -4.1 kV; aperture D1 $= 300\ \mu$m). For the analyses, the focused primary ion beam was rastered over areas of variable size. For most measurements, the spot size, i.e., the area sputtered during analysis, was 2×2, or $3 \times 3\ \mu m^2$, but in some cases we had larger $6 \times 6\ \mu m^2$ spots. Analyses were carried out in either "isotope" mode (2×2, or $3 \times 3\ \mu m^2$ spots; Figure 2) or in "image" mode (3×3, or $6 \times 6\ \mu m^2$ spots). The spatial resolution of analyses in image mode was about 200 nm. The largest spots are useful when analyzing pervasively fractured troilite grains where the precise setting of the analysis spot may be challenging, owing to the low magnification of NanoSIMS' optical microscope and the "poor" reproducibility (1–2 μm) of stage positions between the SIMS and Microscope modes (Figure 3). Ion imaging on such relatively large areas (sometimes also aided by EDX element maps recorded in advance) allows precise selection of fracture-free regions of interest during data reduction. Positive secondary ions of ^{28}Si, ^{46}Ti+^{46}Ca, ^{54}Fe, ^{60}Ni, and ^{62}Ni were measured simultaneously using electron multipliers, for 50–120 minutes (depending on spot size). Peak positions were adjusted automatically every 15 minutes based on the drift of the ^{54}Fe peak. We corrected all raw iron and nickel data by the dynamic background, which we measured the same way as normal analysis points within the same sulfide grain, except that we adjusted the deflection plate voltages by -12 V (Mostefaoui et al. 2005). This corresponds to about -28 mamu (mamu = milli atomic mass unit) at masses 60–62. In the case of both measured nickel isotopes, the intensity of the dynamic background was up to 10% of the signal in troilites with the highest Fe/Ni ratios (Fe/Ni: 1,200,000) and less for troilites richer in nickel. The mass resolution ($M/\Delta M$; Cameca definition, see Hoppe et al. 2013) was between 4000 and 5000 for masses 60 and 62. Isotope and element ratios were calculated from the sums of counts recorded for each isotope. We only used uniform and, as much as possible, nickel-poor signal intervals (Isotope mode) and areas (Imaging mode) to calculate isotope and element ratios. For the external normalization of isotope ratios, we used either the NBS 446 steel standard or sulfide grains from our samples with Fe/Ni ratios below 800. In both cases, we assumed terrestrial nickel isotope composition (Gramlich et al. 1989). Element ratios were calculated using the sensitivity ratios estimated from the measurement of either the NBS 446 steel reference material or nickel-rich sulfides from our samples (nickel content several weight percent, or higher, determined by EPMA or SEM-EDX). Final uncertainties of isotope and element ratios for each spot were propagated from the counting statistics of the given analysis and associated dynamic background, from the uncertainties of isotope and element ratios measured in the reference materials during the same analytical session, and from the uncertainties of the Fe/Ni ratios measured by EPMA or SEM-EDX in the reference materials in advance. In general, sulfide was always preferred to the NBS 446 steel for external normalization, but it was not always possible to use a sulfide as reference material. For example, a sulfide otherwise suitable for external normalization might have been too small for repeated analyses or had a too high Fe/Ni ratio for precise EPMA or SEM-EDX measurements. Each sulfide in our data set whose ^{60}Ni/^{62}Ni ratio was normalized externally to the NBS 446 steel reference material and had a low Fe/Ni ratio ($<$2400; ^{56}Fe/^{62}Ni $\lesssim$ 61,000) shows a terrestrial isotope composition within analytical uncertainty (see Section 4), which gives us confidence in the accuracy of our NBS 446 steel-normalized nickel isotope data. However, the Fe/Ni ratios of nickel-rich sulfides calculated using the NBS steel as an external reference often did not match those measured by EPMA or SEM-EDX analyses (they were a factor of 1.2–3.3 lower than expected). Therefore, we trust more the Fe/Ni ratios calculated with the sensitivity ratios estimated from the measurements of nickel-rich sulfides in our samples (the few exceptions are indicated; see Section 4).

The tail of the ^{46}Ti^{16}O/^{46}Ca^{16}O peak may contribute to the ^{62}Ni signal in analytes with extremely high Ti/Ni ratios (above several hundred), as also noted by Mostefaoui et al. (2005). Monitoring and quantifying this interference in our troilites was difficult because the ^{62}Ni and ^{46}Ti^{16}O/^{46}Ca^{16}O peaks both had very low intensities. Routine mass scans on our troilites did not pick up any ^{46}Ti^{16}O/^{46}Ca^{16}O signal, which means that its peak intensity must have been below 0.05 counts per second (cps). The tail of such a peak would have a negligible effect on the ^{62}Ni signal, even in troilites poorest in nickel (Fe/Ni ratios: 900,000–1,200,000, ^{62}Ni intensity $\sim$0.05 cps). Nevertheless, in order to further minimize, or eliminate, the potential of the ^{46}Ti^{16}O/^{46}Ca^{16}O isobar to bias our measurements, we recorded

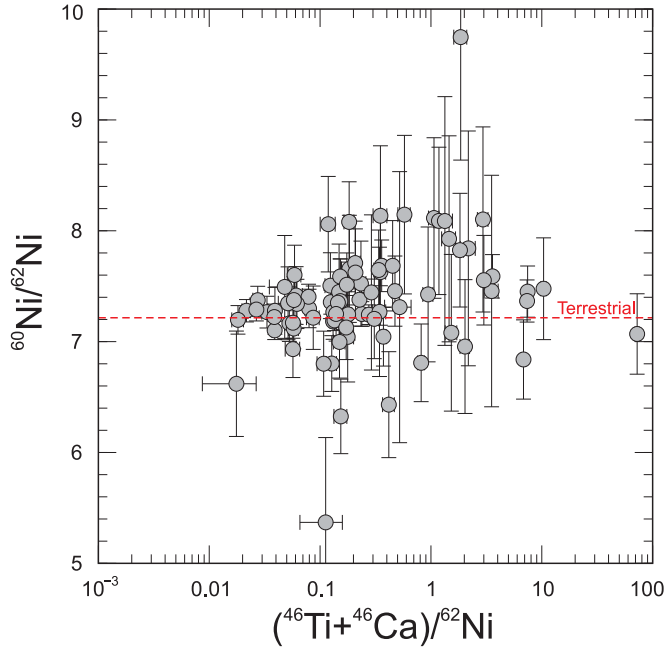

Figure 4. ^{60}Ni/^{62}Ni ratios of chondritic troilite as a function of raw (^{46}Ti $+^{46}$Ca)/^{62}Ni ratios. NanoSIMS data with uncertainties ($\pm 1\sigma$). Note the logarithmic scale of the horizontal axis.

^{62}Ni −0.5 V off the peak center (1.2 mamu) and avoided the titanium/calcium-rich parts of the measurement signal/image. In Figure 4 we plot the raw (^{46}Ti+^{46}Ca)/^{62}Ni ratios measured on our sulfides against their standardized ^{60}Ni/^{62}Ni ratios. The correlation shown by the point cloud is insignificant (correlation coefficient: −0.0075, slope: $-6.07 \pm 48.2 \times 10^{-4}$; linear regression following Mahon 1996), which is also consistent with the effect of the ^{46}Ti^{16}O/^{46}Ca^{16}O peak tail on ^{62}Ni being negligible.

Evaluating and mitigating the potential effects of the ^{59}Co^{1}H isobaric interference on ^{60}Ni was less straightforward. At the mass resolution of our NanoSIMS measurements, the two peaks are not separated completely. The low-mass tail of the ^{59}Co^{1}H peak, if present, is expected to overlap with the ^{60}Ni peak center. Therefore, as a precaution, we routinely measured ^{60}Ni −0.5 V off the peak center (−1.2 mamu), where the intensity of the ^{60}Ni signal is the same as at the ^{60}Ni peak center, but the ^{59}Co^{1}H signal tails off (Figure 5). Because the geometry of NanoSIMS does not allow the simultaneous analysis of ^{59}Co and ^{60}Ni, we had to resort to the evaluation of scans on mass 60 to constrain the effect of the ^{59}Co^{1}H isobar. We performed these mass scans on "cobalt-rich" metal and sulfide grains (cobalt content ∼2 wt% in metal and 0.5–1 wt% in sulfide; wt% = weight percent), as well as nickel-poor troilites of the studied samples. Cobalt-rich metal and sulfide grains tend to be nickel rich, too (tens of wt% nickel), so the ^{59}Co^{1}H peak is on the high-mass flank of the ^{60}Ni peak (Figure 5(a)). Furthermore, the high-mass flank of the ^{59}Co^{1}H peak can potentially be obscured by the peaks of ^{30}Si$_2$, ^{58}Fe^{1}H$_2$, ^{58}Ni^{1}H$_2$, and ^{28}Si^{32}S (Figure 5(a)). Nickel-poor sulfides, such as troilite, are also poor in cobalt (cobalt content 0.08–0.10 wt%), so the intensity of ^{59}Co^{1}H in such minerals is expected to be very low, which again makes it difficult to measure the intensity of the isobar directly. On top of all these difficulties, hydride production can be matrix dependent and even span a range of values within the same material. Nevertheless, we tried to quantitatively estimate the maximum influence of ^{59}Co^{1}H on our results using mass scans on some of our sulfides. Figure 5(a) shows the scan of mass 60 on a nickel-rich sulfide (nickel content 18.50 wt%) that also contains 0.45 wt% cobalt, and in Figure 5(b), we show the high-mass "foot" of the ^{60}Ni peak of the same spot. The top of the ^{60}Ni peak spans 8.2 mamu (solid red horizontal line), whereas the peak edges, i.e., the sections of the signal directly next to the peak top, where, coming from the peak top, the rate of decrease in the signal intensity increases abruptly, are 2.0 mamu on each side (dotted red horizontal line). The ^{59}Co^{1}H peak is completely obscured by the high-mass flank of the ^{60}Ni peak, but based on the shape of the ^{60}Ni peak (Figure 5(a)), most of the ^{59}Co^{1}H peak's high-mass edge should be to the right of the ^{60}Ni peak (dotted green horizontal lines in Figures 5(a) and (b). Based on its similarity to the course of the signal to the left of the ^{60}Ni peak (Figure 5(c)), the signal to the right of the ^{60}Ni peak in Figure 5(b) is probably dominated by the ^{60}Ni peak tail, to which a series of overlapping isobar peaks are potentially added. Assuming that the part of the signal closest to the ^{60}Ni peak's "foot" represents the edge of the ^{59}Co^{1}H only, we can estimate the maximum ^{59}Co^{1}H intensity because, based on the ^{60}Ni peak itself, the average intensity of the peak edge at this interval should be about 86% of that of the peak top. The maximum ^{59}Co^{1}H intensity can thus be estimated to be 9.3 ± 3.4 cps in this example. Given the ^{59}Co peak intensity of 5350 cps on the same spot (calculated from two mass scans on the same detector at mass 59 before and after the mass scan at mass 60, after adjusting the magnetic field each time), the hydride production (i.e., ^{59}Co^{1}H/^{59}Co) is 1.75 (± 0.64) $\times 10^{-3}$ at most (as the left, low-mass tail of the ^{60}Ni peak was scanned after the right, high-mass tail, and the ^{60}Ni intensity decreased with time). The ^{54}Fe and ^{59}Co intensities together with the EPMA data of this sulfide allow the estimation of the Fe/Co sensitivity ratio as well (1.426 ± 0.061). Figure 5(d) shows the mass spectrum around mass 60 on a nickel-poor troilite from DOM 08006 before analysis (region of interest b1, spot tro4). This troilite is fairly representative of the nickel-poor troilites in our data set. According to EPMA data, it has an atomic Fe/Co ratio of 730 ± 130 (Co content 0.088 wt%), and nickel is below the EPMA detection limits. Whereas the ^{60}Ni peak is well distinguishable in the spectrum, the ^{59}Co^{1}H peak or its high-mass peak edge are not, due to their extremely low intensity. This spectrum is very similar to those we recorded on other nickel-poor troilites. The maximum ^{59}Co^{1}H signal in this nickel-poor troilite can be calculated using the Fe/Co sensitivity ratio and ^{59}Co^{1}H production estimated above (2.39 ± 0.91 cps). Because the ^{60}Ni peak top does not overlap with the ^{59}Co^{1}H peak top but is instead located at smaller masses than the left, low-mass, ^{59}Co^{1}H peak edge, and, as mentioned above, we routinely analyzed ^{60}Ni −1.2 mamu off the peak center (Figure 5(d)), the ^{59}Co^{1}H intensity at the mass used for actual isotope measurements is much lower than the above estimates. Based on the mass versus intensity relationship seen for ^{60}Ni (Figures 5(a)–(c)), the intensity of the ^{59}Co^{1}H signal at the mass where the ^{60}Ni measurements were performed should be about 1% of its intensity at the ^{59}Co^{1}H peak top. This suggests that the maximum intensity of the ^{59}Co^{1}H signal where we normally measure ^{60}Ni is 0.026 ± 0.01 cps in our typical nickel-poor troilites. This is about a factor of 20 smaller than the typical count rates of our most nickel-poor troilites (0.5 cps), and again, our estimation of

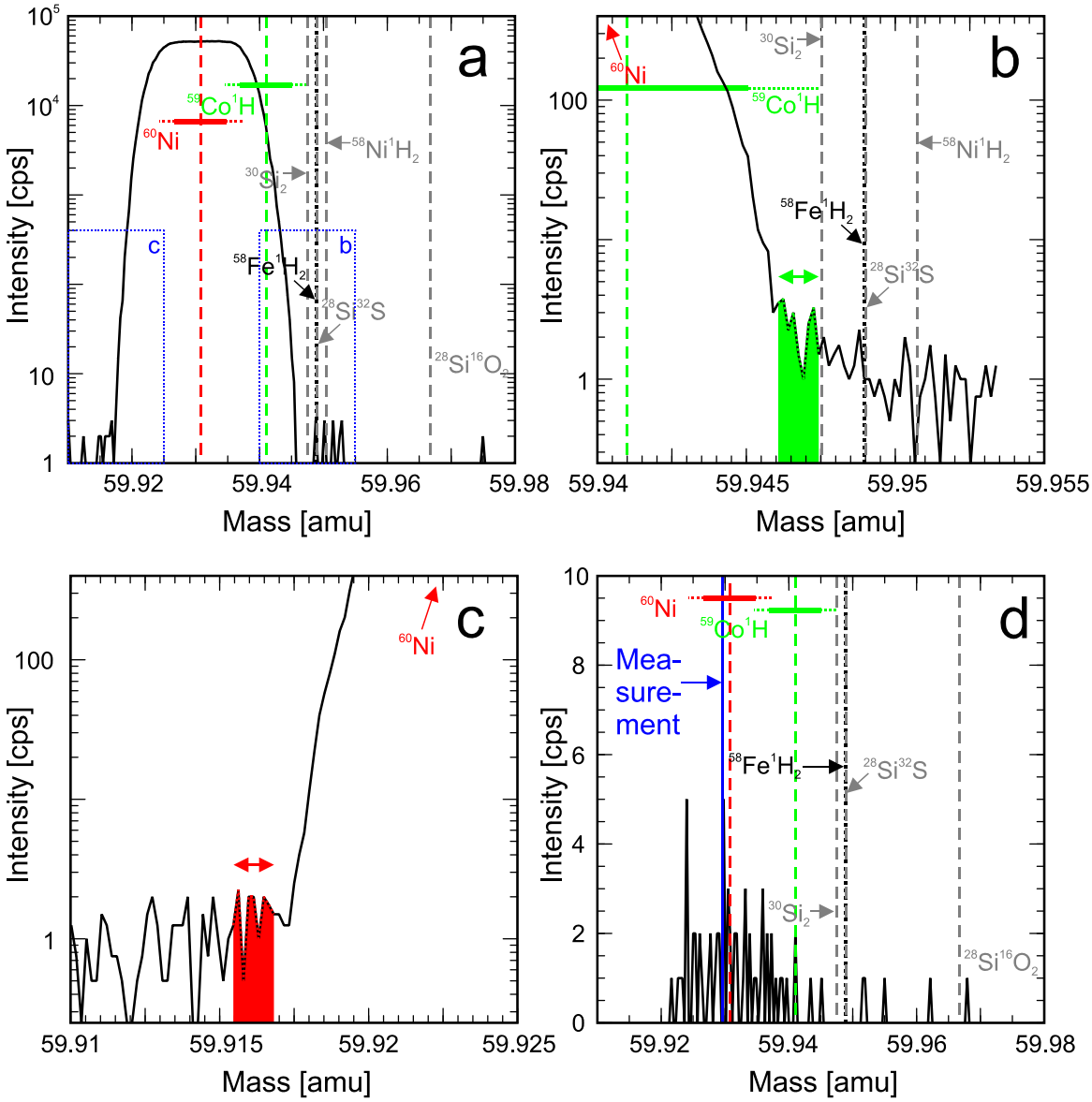

Figure 5. NanoSIMS mass scans around mass 60, recorded over $3 \times 3\ \mu m^2$ measurement fields. Nickel-60 and the major possible isobaric interferences are indicated by dashed vertical lines, except for $^{58}Fe^{1}H_2$ (dotted). Mass intervals of the peak tops and shoulders of ^{60}Ni and $^{59}Co^{1}H$ are indicated by solid and dotted horizontal lines, respectively. (a) Nickel-rich sulfide in DOM 08006, region of interest b30. (b) The high-mass tail of the ^{60}Ni peak at the same spot where (a) was recorded. (c) The low-mass tail of the ^{60}Ni peak at the same spot where (a) was recorded. In (b) and (c) the signal intervals used to estimate the intensity of the (obscured) $^{59}Co^{1}H$ peak are indicated with arrows and coloring. (The interval in (c) was used to estimate the ^{60}Ni tail intensity.) (d) Nickel-poor troilite in DOM 08006, region of interest b1. The mass used for the actual measurement is indicated by a solid blue vertical line.

hydride production is conservative, because it maximizes the interference intensity (see above), so we consider the contribution of the $^{59}Co^{1}H$ isobar to the ^{60}Ni signal in our measurements to be negligible, and the same holds for all the other isobaric interferences at mass 60 mentioned above because these are at masses several mamu higher than $^{59}Co^{1}H$.

3.3. Transmission Electron Microscopy

Electron-transparent slices of three of the troilite grains analyzed by NanoSIMS were prepared with an FEI Nova 600 Nanolab dual-beam focused ion beam instrument (FIB–SEM) at the Max Planck Institute for Polymer Research (Mainz, Germany) and subsequently investigated with the aberration-corrected (objective system) FEI/ThermoFisher Themis transmission electron microscope (TEM) at the UM, operated with an acceleration voltage of 300 kV. The TEM is equipped with a high-brightness field emission gun (X-FEG), a Wien-filter type monochromator, a four-quadrant silicon-drift EDX detector (SuperX technology), a Fischione Model 6000 high-angle annular dark-field (HAADF) detector, and a fast CMOS camera (Ceta 4k × 4k). We performed conventional bright-field, high-resolution imaging and selected area electron diffraction (SAED) to document the texture and crystallography of the studied samples. Spectrum images were acquired in scanning TEM (STEM) mode (condenser aperture 50 μm) using beam currents of about 500–800 pA and analysis times of 100–200 μs/px, with several hundred frames summed up to achieve sufficient counting statistics. EDX quantification was performed using the ThermoFisher Velox software.

4. Results

4.1. Petrography

Troilite grains in different textural contexts were chosen for isotope analysis. Troilite within or on the rims of chondrules, which forms direct, curved interfaces with the chondrules' silicate phases (usually the mesostasis; Figures 6(a) and (b)) and occurs either as pure troilite blebs or together with nickel-rich sulfide (and in one case, with nickel-rich metal), is referred to here as a "chondrule troilite." Chondrule troilite grains found within the chondrules are up to ~80 μm in their longest dimension. Troilite found on the rims of Type I chondrules is often associated with magnetite, iron-rich olivine (few-micron crystals with 25–55 mole% fayalite content; Figures 6(c)–(e)), and sometimes other silicate (e.g., calcium-rich pyroxene) and oxide (chromium-rich hercynite) phases, besides nickel-rich sulfide. The silicate and hercynite companions of such troilites often form micro- or cryptocrystalline mixtures with troilite (crystal diameters between tens of nanometers and a few thousand nanometers), and sometimes line the contact between troilite and the host chondrule's silicates (Figure 6(d)). Rarely, the iron-rich olivine has diffuse zoning, with increasing iron content toward the rim. The troilite ± olivine ± magnetite ± nickel-rich sulfide ± calcium-rich pyroxene ± hercynite assemblages along chondrule rims do not extend into the matrix along veins, and they have sharp boundaries with the neighboring matrix, which, in the case of chondrule fragments, cut the boundary between chondrule silicates and the associated troilite rim (Figure 6(e)). A similar, fine-grained troilite–olivine mineral assemblage (with calcium-rich pyroxene and melilite in addition) was also found surrounding a CAI in DOM 08006. Troilite from these assemblages is referred to as "rim troilite" in our data tables. Finally, we found troilite suitable for NanoSIMS analysis occupying space between chondrules. They are the major phases of sulfide ± metal assemblages that are 20–100 μm in diameter, i.e., smaller than the diameter of most chondrules and so-called opaque assemblages (see Alpert et al. 2021) in the studied samples (a few hundred to several hundred microns). We refer to such troilite grains as "matrix troilites," although their grain size distinguishes them from the sensu stricto meteorite matrix (grain size <5 μm). Some of these sulfide grains have convex boundaries with the surrounding matrix (Figure 6(f)). However, others have round outlines, suggestive of a spherical form in three dimensions (Figure 6(g)). Phases most commonly occurring together with matrix troilite are Ni-rich sulfide and nickel-rich metal (Ni: 50–60 wt%; Table 2). Nickel-rich sulfide is not uniformly distributed within the matrix troilite grains targeted for NanoSIMS analysis, but it is concentrated in single sulfide masses in contact with troilite. Nickel-rich metal, if present, is volumetrically subordinate (Figure 6(g)).

The only chondrule troilite analyzed so far with TEM (region of interest Ch3 from MET 00526; Figure 7(a)) has a 2C troilite structure (space group P-62c). However, some SAED patterns recorded from its [120] zone axis contain faint series of diffuse points along the reciprocal c-axis, which may indicate the presence of small amounts of pyrrhotite (Figure 7(a)). Unfortunately, we do not have electron microprobe data for this troilite, and metal/S ratios determined with STEM-EDX are probably not accurate (e.g., they indicated metal/S ratios >1 for matrix troilite, but microprobe data available for that troilite suggested metal/S ratios <1), so we do not have information about cation deficiency that could support the potential presence of pyrrhotite. Transmission electron microscopy of one rim and one matrix troilite (regions of interest: b15 and b16, respectively, from DOM 08006; Figures 6(c) and (g) showed that these troilites have well-ordered 2C structure (Figure 7(b)) with no detectable intergrown pyrrhotite. Rim troilite in b15 appears to have the same orientation within the FIB slice, regardless of the presence of associated phases. In places where troilite occurs together with iron-rich olivine, the latter has triple junctions (Figure 8(a)), and chromium-rich hercynite occurs between and within troilite and iron-rich olivine crystals (Figure 8(b). Matrix troilite in b16 (Figures 6(g) and 8(c)) has iron-oxide (presumably magnetite) inclusions of various size (<100 nm to 1.5 μm in longest dimension; Figure 8(d)). These oxide inclusions are not connected to either the surface or the nickel-rich metal of the host sulfide-metal grain.

Some of the analyzed troilites are fractured (Figures 3, 6(a), 9(a), and 9(b)). In some cases, the fractures have fillings that contain silicon, oxygen ± aluminum ± alkaline earth metals ± sodium ± iron ± nickel (Figure 9(c)). We speculate that the fillings may contain iron- and/or nickel-bearing sheet silicates and metal-oxy-hydroxide phases. Filled fractures have a thickness between a few tens of nanometers up to a few hundred nanometers. Although the presence of all but the thinnest veins is noticeable in ion images, we documented our NanoSIMS analysis spots after isotope measurements using BSE imaging to see if the analyzed spot or region of interest accidentally included fractures or veins that were not visible in ion images. In the case of isotope analyses in isotope mode, temporal changes of isotope signals may or may not reveal the presence of fractures, veins, or inclusions within the analyzed volume. Thus, here, too, an inspection of NanoSIMS measurement pits was necessary. Analysis points that were found after analysis to contain cracks or inclusions, which we could not see in ion images or notice in the temporal change of ion signals, are not considered hereafter.

4.2. Mineral Chemistry

Based on EPMA data (of which a representative set is provided in Table 2), troilites that occur in the textural contexts detailed above are close to stoichiometric. Their formula is $(Fe,Co,Ni)_{1-x}S$ with x between 0.000 and 0.048. Cobalt contents are between 0.064 ± 0.015 and 0.158 ± 0.019 wt%. (Note that we do not have EPMA results for MET 00526 or QUE 97008.) According to the EPMA measurements, the atomic Fe/Ni ratios of the troilites later analyzed by NanoSIMS varied between 50 and 11500 (if nickel concentration was above the detection limit) but were usually between 2000 and 3000. Our NanoSIMS data indicate not only similar but also much higher Fe/Ni ratios, up to about 1,200,000 ($^{56}Fe/^{62}Ni \approx 30{,}000{,}000$; Table 3; Figures 10 and 11). The most likely reasons why apparent Fe/Ni ratios obtained by NanoSIMS were higher than those measured by EPMA are (1) that the excitation volume of EPMA spots can be larger than the volume sampled during NanoSIMS measurements (this is especially true in the case of the 2×2 μm^2 spot analyses) and (2) that submicron-scale nickel heterogeneities are averaged out by EPMA, whereas NanoSIMS ion imaging allows the precise definition of regions of interest with a homogeneously low nickel content. Based on

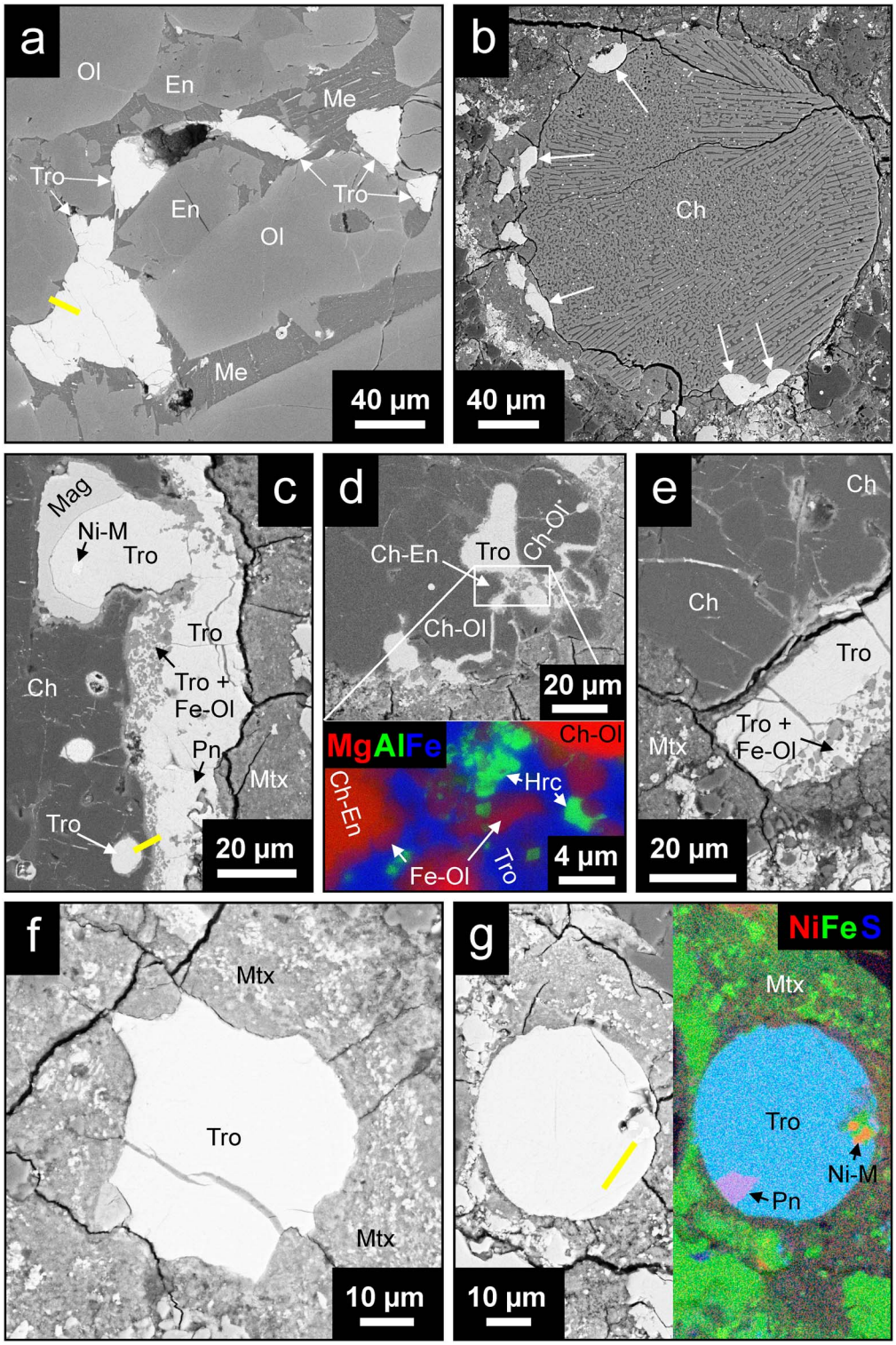

Figure 6. Typical textures of chondritic troilites selected for isotope analysis. Abbreviations: Tro = troilite, Me = mesostasis, En = enstatite, Ol = olivine, Fe-Ol = iron-rich olivine, Ch = chondrule, Mag = magnetite, Pn = pentlandite, Ni–M = nickel-rich metal, Mtx = meteorite matrix, Hrc = hercynite. (a)–(b) "Chondrule troilite" (BSE images). (a) Detail of a porphyritic olivine–pyroxene chondrule in MET 00526 (region of interest: Ch3), with troilite blebs "squeezed" between olivine and enstatite, and curved boundaries between troilite and mesostasis. The yellow line indicates the position of the FIB slice shown in Figures 7 and 9. (b) Troilite ± pentlandite (arrows) along the outer rims of a radial olivine chondrule in DOM 08006 (region of interest: b46). Notice again the curved boundaries between sulfide and silicate (gray), which suggests that sulfide and silicate were once two coexisting liquids. Most of the bright spots inside the chondrule are troilite grains. (c)–(e) "Rim troilite." (c) Porphyritic olivine–pyroxene chondrule in DOM 08006 (region of interest: b15), with a rim consisting of troilite, magnetite, pentlandite, iron-rich olivine (fayalite content ≈50%), and nickel-rich metal (nickel content ≈50 wt%). The yellow line indicates the approximate position of the FIB slice shown in Figures 8(a) and (b) (BSE image). (d) Troilite with iron-rich olivine (fayalite content ≈40%) and chromium-rich hercynite on the edge of a porphyritic olivine–pyroxene chondrule in DOM 08006 (region of interest: b1). BSE image (top) and composite SEM-EDX element map (bottom). Note that the interface between troilite and the host chondrule's phases (Ch-En, Ch-Ol) is lined with silicates and oxides. (e) Troilite and iron-rich olivine (fayalite content ≈25%–44%) on the edge of a chondrule fragment in ALHA77307 (region of interest: b7) (BSE image). (f)–(g) "Matrix troilite." (f) "Large" troilite grain in the fine-grained matrix of ALHA77307 (region of interest: b9) (BSE image). (g) BSE image (left) and composite SEM-EDX element map (right) of a spherical metal-sulfide assemblage in DOM 08006 (region of interest: b16). The yellow line indicates the approximate position of the FIB slice shown in Figures 8(c) and (d).

Table 2
Representative Set of Sulfide and Metal Compositions

Sample	Area of Interest	Mineral	Textural Type[a]	Measurement	S (wt.%)	±	Fe (wt.%)	±	Co (wt.%)	±	Ni (wt.%)	±	O (wt.%)	±
Semarkona	b4	Tro	m	tro2	35.85	0.09	62.19	0.09	0.109	0.011	0.065	0.012	0.35	0.02
	b14	Tro	ch	2-tro1	36.44	0.17	61.89	0.26	0.108	0.018	0.067	0.019	b.d.l.	
	b14	Tro	ch	3-tro1	36.62	0.18	61.23	0.26	0.116	0.018	0.057	0.019	b.d.l.	
	b16-17	Tro	ch	tro8	37.01	0.35	61.01	0.52	0.108	0.015	0.189	0.017	0.10	0.03
	b16-17	Tro	ch	tro10	36.98	0.36	61.20	0.52	0.097	0.015	0.014	0.016	0.31	0.03
	b16-17	Tro	ch	tro2	37.04	0.36	61.33	0.52	0.109	0.015	0.006	0.016	0.28	0.03
DOM 08006	b1	Tro	rim	tro5	36.86	0.35	61.62	0.52	0.093	0.016	b.d.l.		0.38	0.03
	b13	Tro	m	tro2	36.98	0.36	61.46	0.52	0.098	0.016	b.d.l.		0.48	0.03
	b15	Tro	rim	tro7	37.09	0.36	61.40	0.52	0.092	0.016	b.d.l.		0.43	0.03
	b16	Tro	m	tro6	37.03	0.36	62.03	0.52	0.095	0.015	0.049	0.016	0.29	0.03
	b16	Pn	m	pn7	33.57	0.34	46.48	0.44	0.734	0.020	19.109	0.071	0.47	0.03
	b16	Ni–M	m	nim9	0.10	0.03	37.55	0.38	1.625	0.026	60.130	0.120	0.93	0.02
	b46	Tro	ch	tro2	35.68	0.25	61.40	0.37	0.100	0.018	0.047	0.020	0.66	0.06
	b47	Tro	ch	tro2	36.60	0.25	61.37	0.37	0.095	0.018	0.014	0.020	0.71	0.06
ALHA77307	b4	Tro	ch	tro1	36.94	0.25	61.74	0.37	0.107	0.018	0.007	0.020	0.33	0.05
	b4	Tro	ch	tro2	35.86	0.25	62.46	0.37	0.097	0.017	0.022	0.020	0.62	0.06
	b5	Tro	m	tro3	36.71	0.25	61.80	0.37	0.085	0.018	0.027	0.020	0.42	0.06
	b7	Tro	rim	tro3	36.72	0.25	61.73	0.37	0.091	0.018	0.013	0.020	0.43	0.06
	b7	Tro	rim	tro15	36.51	0.25	61.99	0.37	0.096	0.018	0.014	0.020	0.43	0.05
	b9	Tro	m	tro1	36.81	0.25	61.95	0.37	0.107	0.018	0.018	0.020	0.26	0.05
	b9	Tro	m	tro3	36.83	0.25	61.93	0.37	0.103	0.018	0.028	0.020	0.50	0.06

Sample	Area of Interest	Mineral	Textural Type[a]	Measurement	Mn (wt.%)	±	Cr (wt.%)	±	Cu (wt.%)	±	Zn (wt.%)	±	Ti (wt.%)	±
Semarkona	b4	Tro	m	tro2	n.a.		0.038	0.009	n.a.		n.a.		n.a.	
	b14	Tro	ch	2-tro1	0.006	0.018	0.040	0.014	b.d.l.		b.d.l.		n.a.	
	b14	Tro	ch	3-tro1	b.d.l.		0.036	0.014	b.d.l.		0.001	0.034	n.a.	
	b16-17	Tro	ch	tro8	0.008	0.015	0.025	0.013	0.008	0.023	0.013	0.031	n.a.	
	b16-17	Tro	ch	tro10	0.003	0.015	0.021	0.013	0.006	0.024	0.004	0.031	n.a.	
	b16-17	Tro	ch	tro2	0.006	0.015	0.018	0.013	b.d.l.		b.d.l.		n.a.	
DOM 08006	b1	Tro	rim	tro5	0.022	0.015	0.069	0.015	b.d.l.		0.016	0.031	n.a.	
	b13	Tro	m	tro2	0.017	0.015	0.013	0.014	b.d.l.		0.007	0.030	n.a.	
	b15	Tro	rim	tro7	0.000	0.014	0.079	0.015	0.005	0.024	b.d.l.		n.a.	
	b16	Tro	m	tro6	b.d.l.		0.015	0.013	0.003	0.024	b.d.l.		n.a.	
	b16	Pn	m	pn7	0.008	0.015	0.021	0.014	0.008	0.025	b.d.l.		n.a.	
	b16	Ni–M	m	nim9	0.005	0.015	0.025	0.014	0.030	0.028	b.d.l.		n.a.	
	b46	Tro	ch	tro2	0.018	0.026	0.135	0.016	0.028	0.024	0.009	0.031	0.001	0.011
	b47	Tro	ch	tro2	0.018	0.027	0.054	0.014	0.025	0.024	b.d.l.		0.003	0.012
ALHA77307	b4	Tro	ch	tro1	0.011	0.034	0.012	0.014	0.030	0.024	0.023	0.031	0.009	0.012
	b4	Tro	ch	tro2	0.020	0.025	0.064	0.014	0.003	0.024	0.023	0.031	0.006	0.012
	b5	Tro	m	tro3	0.003	0.004	0.027	0.014	0.012	0.024	b.d.l.		0.004	0.012
	b7	Tro	rim	tro3	0.010	0.031	0.048	0.014	0.012	0.024	0.021	0.031	0.004	0.012
	b7	Tro	rim	tro15	0.005	0.030	0.025	0.014	0.006	0.024	b.d.l.		0.0001	0.020
	b9	Tro	m	tro1	0.009	0.051	0.030	0.014	0.018	0.024	0.008	0.031	0.002	0.012
	b9	Tro	m	tro3	0.004	0.008	0.056	0.015	b.d.l.		0.008	0.031	0.006	0.012

Note. EPMA data; b.d.l. = below detection limit; n.a. = not analyzed
[a] ch = chondrule, m = matrix, rim = sulfide occurring with iron-rich olivine in chondrule and CAI rims; see the Results section for details on classification.

NanoSIMS data, troilite Fe/Ni ratios in ordinary chondrites do not extend above about 40,000 ($^{56}Fe/^{62}Ni \approx 1{,}000{,}000$; Figures 10 and 11), whereas Fe/Ni ratios three times as high are common in the troilites of the two carbonaceous chondrites. This holds true even if we disregard data that were obtained with NBS 446 as the external reference used to estimate the Fe/Ni sensitivity ratio.

4.3. Isotope Compositions

NanoSIMS isotope data are listed in Table 3. $^{60}Ni/^{62}Ni$ ratios are between 5.37 ± 0.77 and 9.75 ± 1.11. Out of the 86 measured $^{60}Ni/^{62}Ni$ ratios, 6 were anomalous relative to the terrestrial composition by $>2\sigma$ (two being lower, four higher than the terrestrial ratio), but none of the measured $^{60}Ni/^{62}Ni$ ratios is anomalous at the 99.7% confidence level. These statistics are close to what is expected in such a data set if the analyzed troilites had a terrestrial isotope composition and measured variations were merely stochastic. The weighted average of $^{60}Ni/^{62}Ni$ ratios is not terrestrial at $\geqslant$95% confidence level (7.270 ± 0.020; $\chi^2 = 1.06$; the terrestrial ratio is 7.215 ± 0.003; Gramlich et al. 1989). To check whether small nickel-60 anomalies from in situ iron-60 decay may be present in our data set, we performed a weighted linear regression of $^{60}Ni/^{62}Ni$ and $^{56}Fe/^{62}Ni$ ratios to calculate $^{60}Fe/^{56}Fe$ ratios at formation. Weighted linear regression of $^{60}Ni/^{62}Ni$ and $^{56}Fe/^{62}Ni$ ratios of individual troilite grains is often not possible or sensible, however, owing to the small number of analysis points, in many of our grains. Furthermore, as detailed in Section 3.2, $^{56}Fe/^{62}Ni$ ratios estimated using the Fe/Ni sensitivity ratios calculated from NBS 446 measurements are not necessarily accurate. Linear regression of data (Mahon 1996) with "accurate" $^{56}Fe/^{62}Ni$ ratios (see Section 3.2, and Table 3) gives an average estimated $^{60}Fe/^{56}Fe$

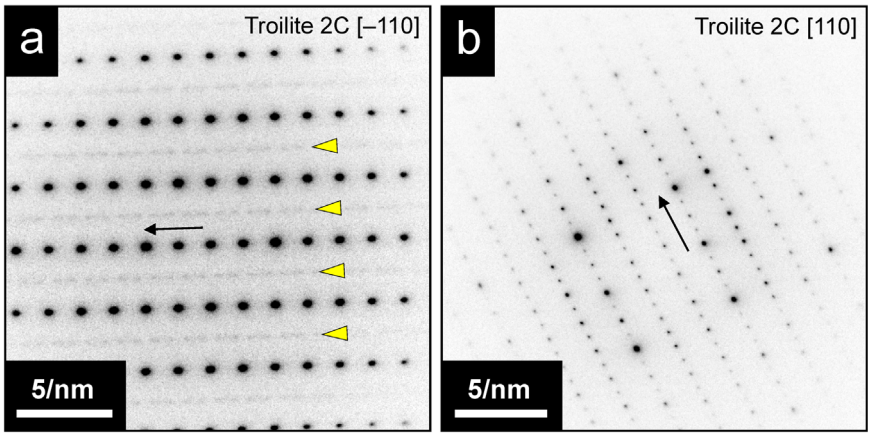

Figure 7. (a) SAED pattern of the chondrule troilite from MET 00526 displayed in Figure 6(a). The black arrow indicates the orientation of the reciprocal *c*-axis. Yellow triangles point at the series of diffuse diffraction spots possibly resulting from small amounts of pyrrhotite intergrown with troilite. Note that the image brightness was increased significantly before the tones were inverted, so the "pyrrhotite" reflections would not be visible in the original image. (b) SAED pattern of the rim troilite depicted in Figure 6(c) (meteorite DOM 08006, region of interest: b15). Arrow indicates the orientation of the reciprocal *c*-axis.

of $1.05(\pm1.48) \times 10^{-8}$ ($n = 45$; $\chi^2 = 0.99$; Figure 12). The estimated average initial $^{60}Fe/^{56}Fe$ ratio of chondrule troilites is also indistinguishable from zero given the uncertainties (-3.24 $(\pm5.94) \times 10^{-8}$; $n = 20$; $\chi^2 = 1.22$; again, only data with "accurate" Fe/Ni ratios were considered), as are the initial $^{60}Fe/^{56}Fe$ ratios estimated from rim (-0.34 $(\pm3.97) \times 10^{-8}$; $n = 6$; $\chi^2 = 0.28$) and matrix troilite data (3.33 $(\pm2.26) \times 10^{-8}$; $n = 19$; $\chi^2 = 1.02$).

5. Discussion

5.1. Origin of the Studied Troilites

Key to the interpretation of our isotope data is the origin of the analyzed troilites. As mentioned in Section 2, our aim was to find troilites with a high-temperature origin and short cooling time so that it could be reasonably assumed that, in the absence of thermal metamorphism or aqueous alteration, their Fe/Ni ratios and nickel isotope compositions had only been influenced by iron-60 decay since their formation.

Chondrule troilites have convex boundaries toward the chondrule mesostasis and, occasionally, toward other chondrule phases (Figures 6(a) and (b)). The formation of such chondrule troilites is either linked to exsolution from sulfide oversaturated chondrule melts (Rubin et al. 1999; Marrocchi & Libourel 2013) or, when occurring on the rims of chondrules, to the replacement of solid chondrule metal by sulfide (Zanda et al. 1997; Lauretta & Buseck 2003; Schrader et al. 2008). Sulfide oversaturation can occur after the chondrule melt's sulfur and silica contents have increased through reaction with sulfur- and silicon-rich gas. The replacement of chondrule metal by sulfide is expected when the chondrule and the surrounding gas cool sufficiently for gaseous sulfur species to react with the metal. In the latter case, nickel-rich metal and phosphides ± fayalitic olivine are also expected to form (Lauretta & Buseck 2003; Schrader & Lauretta 2010). We found no phosphides together with our chondrule troilites, and only one chondrule where chondrule troilite was accompanied by nickel-rich metal (region of interest b47 in DOM 08006). Furthermore, we have not been able to find metal blebs of similar size and shape to those of our chondrule troilites within the same host chondrules either. However, in two chondrules with chondrule troilite (regions of interest Ch3 and b46 in MET 00526 and DOM 08006, respectively), we found evenly distributed, minute (⩽few microns) troilite grains that precipitated within the mesostasis upon final quenching, attesting to the presence of sulfur within the chondrule melts. We therefore find it unlikely that our chondrule troilites formed through the reaction of solid metal with sulfur-bearing gas upon chondrule cooling. Instead, they were probably formed by exsolution from chondrule melts.

The origin of rim troilites is a bit more ambiguous. The texture of rim troilites is similar to that of chondrule troilites that occur close to or on the rims of chondrules (convex boundaries, round or amoeboid shape; Figures 6(c) and (d)). However, rim troilite occurs, besides other phases, together with iron-rich olivine (forsterite content 45–75 mole%) that is clearly not in equilibrium with the iron-poor olivines and pyroxenes of the host chondrules (forsterite and enstatite content above mole 90%). Thus, rim troilite is not part of the original chondrule mineral assemblage. Fayalite (forsterite content below 50%), with or without hedenbergite, magnetite, saponite, and troilite, has been observed in assemblages of various sizes and shapes, including veins, in carbonaceous chondrites that underwent low-temperature ($T < 150$°C) aqueous alteration at low water/rock ratios (<1; Krot et al. 2000; Jogo et al. 2009; Tomeoka & Ohnishi 2014; Suttle et al. 2022). However, a hydrothermal origin seems unlikely in the case of our rim assemblages because our rim troilite never forms veins that extend into the surrounding matrix, and the mineral assemblage of our rim troilites also includes euhedral, chromium-rich hercynite (Figures 6(d) and 8(b)), which is absent among the aqueous alteration products generally observed. In the fine-grained troilite–olivine intergrowths (top of Figure 8(a)), troilite and olivine have ∼120° triple junctions (inset of Figure 8(a)), indicating about coeval formation of these phases. Euhedral, chromium-rich hercynite occurs within and outside troilite and olivine, which suggests that either its crystallization preceded those of olivine and troilite, or it had a higher nucleation rate than those of olivine and troilite. This texture, which resembles the poikilitic texture of magmatic rocks, is most consistent with crystallization from a melt. The simplest scenario explaining the formation of these melts is short-term heating of a troilite ± metal ± silicate-bearing original mineral assemblage, i.e., chondrule troilite ± metal, or troilite-rich fine-grained chondrule rims, by flash heating or impact shock. Sulfide melted completely, but only very limited

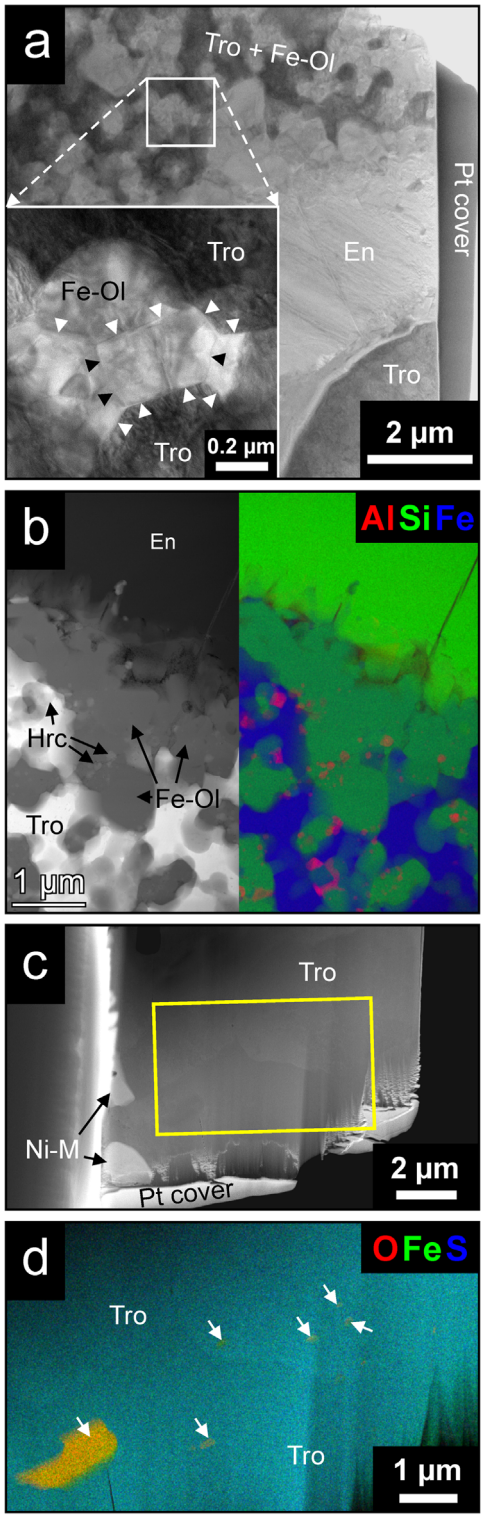

Figure 8. Details of troilite-bearing assemblages. For abbreviations, see Figure 6. (a) TEM bright-field image of an FIB slice of the chondrule rim shown in Figure 6(c) (meteorite DOM 08006, region of interest: b15). The boundaries of individual submicron iron-rich olivine and troilite crystals (marked by arrowheads) have ~120° triple junctions. (b) STEM-HAADF image (left) and composite SEM-EDX element map (right) of a detail of the FIB slice shown in (a). (c) STEM-HAADF image of the FIB slice lifted from the sulfide + metal assemblage displayed in Figure 6(f) (meteorite DOM 08006, region of interest: b16). The yellow rectangle shows the area depicted in (d). (d) STEM-EDX element map of the FIB slice shown in (c). One large and several small iron-oxide inclusions (orange) are marked by arrows.

melting occurred in the chondrule silicates, either because the temperature was not high enough for complete melting and/or because of kinetic reasons. The small amount of silicon and refractory elements, such as aluminum, calcium, and chromium, that entered the sulfide melt from the chondrule silicates, started to quickly crystallize, most prominently close to their sources, i.e., along the troilite–chondrule enstatite and troilite–chondrule olivine boundaries (Figures 6(c), (d), and 8(a), but the resulting silicates were much richer in iron than the chondrule silicates because of the abundant iron that was available in the sulfide melt. In summary, the origin of rim troilites studied here is not completely clear, but crystallization from a melt appears to be more likely than a hydrothermal origin. Regardless, rim troilite postdates its host chondrules and CAIs, but chondrules and rim troilites were associated before the final assembly of the meteorite parent bodies. This is attested to by chondrule fragments with rim troilite, where the boundary between chondrule silicates and the associated troilite rim are cut by the matrix (Figure 6(e)).

Matrix troilites probably do not share a single origin, but many of them have some common features that may provide constraints on their formation conditions. Matrix troilites chosen for isotope analysis are either monomineralic or occur together with nickel-rich sulfide (in most cases close to stoichiometric pentlandite) ± nickel-rich metal. Where present, nickel-rich metal associated with matrix troilite is volumetrically subordinate (e.g., region of interest b16 in DOM 08006; Figure 6(g)). Qualitatively, the mineral assemblage in which matrix troilite occurs is similar to that expected upon nebular sulfurization of kamacite (troilite + pentlandite ± nickel-rich metal; Lauretta et al. 1998; Schrader & Lauretta 2010). Some of the troilite + nickel-rich sulfide ± nickel-rich metal assemblages are rounded with no sign of corrosion on the edges, which indicates that the round form of these objects is original. Such grains thus represent quenched melt droplets (only a liquid can minimize its surface by developing a spherical form; a solid would have to develop crystal faces). If they were the products of in situ replacement of round metal grains, they would not have been able to retain their shape because of the volume increase associated with sulfide growth (see Lauretta et al. 1997; Schrader & Lauretta 2010). The melting and quenching of these sulfides likely happened in a nebular setting because they would not have been able to become spherical if melting had occurred on the parent body. They are most likely the products of high-temperature ($\gtrsim$1000°C) sulfurization of kamacite, which is accompanied by sulfide melt formation. Matrix troilite grains with irregular shapes (Figure 6(f)) may be broken pieces of larger quenched melt droplets, or they are fragments of chondrule troilite or rim troilite grains.

In summary, the troilites analyzed here are most likely the products of high-temperature processes that probably took place in a nebular setting. However, in the case of rim troilites, if they were formed by impact shock, formation on the parent body with subsequent transport through impact gardening cannot be ruled out completely.

5.2. No Resolvable Signs of In situ Iron-60 Decay

The analyzed troilites showed no discernible enrichment in nickel-60 as a result of in situ iron-60 decay, either on average or individually. The inferred average initial $^{60}Fe/^{56}Fe$ ratio of

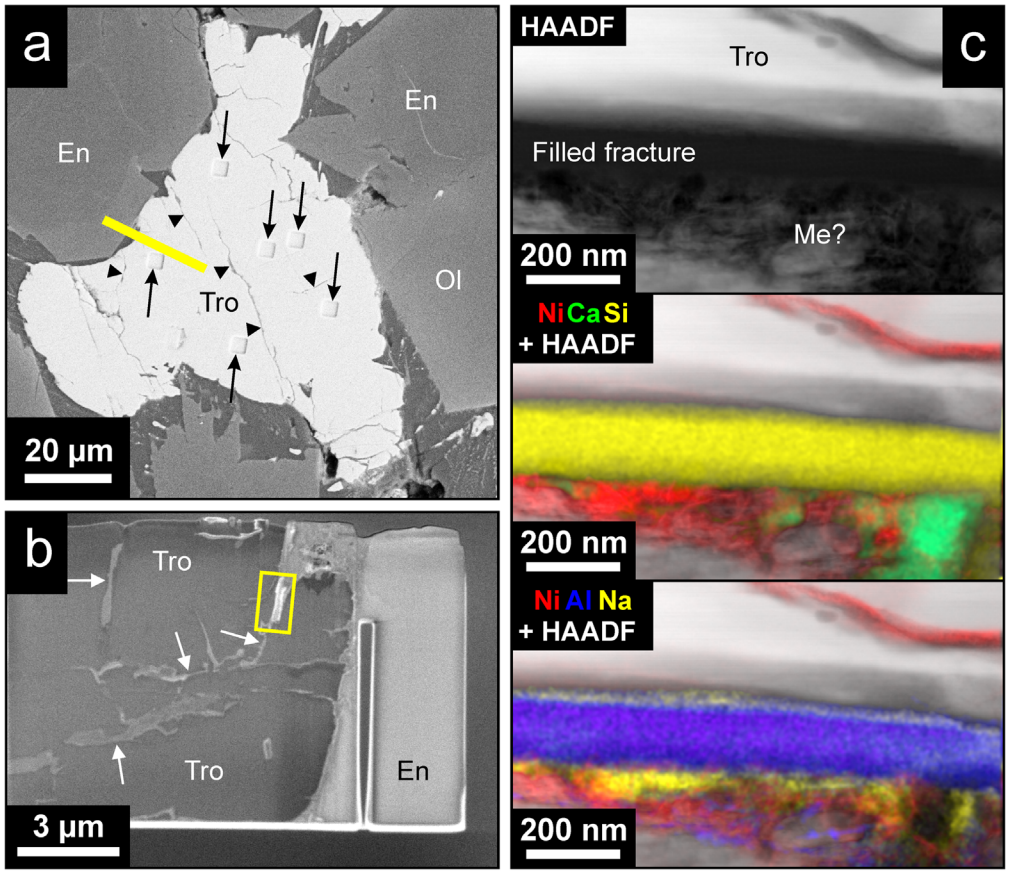

Figure 9. Fractures in a chondrule troilite from MET 00526 (region of interest: Ch3). For abbreviations, see Figure 6. (a) Backscattered electron image of troilite with NanoSIMS analysis pits (black arrows). Some fissures cross-cutting the troilite surface are marked with arrowheads. The yellow line indicates the approximate position of the FIB slice shown in (b) and (c). (b) SE image of the FIB slice of the troilite displayed in (a) at the end of the FIB preparation. Fissures (white arrows) can be observed cutting through the troilite, some with filling. The yellow rectangle indicates the area depicted in (c). Abbreviations are the same as in (a). (c) HAADF (top) and composite HAADF-element (STEM-EDX) images (center and bottom), showing element distribution in the fractures.

our troilites is not significantly larger than zero ($1.05 (\pm 1.48) \times 10^{-8}$; Figure 12). Even without the data obtained on rim troilites, which have an uncertain origin (see above), the average initial $^{60}Fe/^{56}Fe$ ratio of our troilites remains unresolved from zero ($1.75 (\pm 1.83) \times 10^{-8}$). Our results are thus consistent with the $^{60}Fe/^{56}Fe$ ratios inferred from bulk samples (10^{-9}–10^{-8}; Figures 1 and 12) and with the initial $^{60}Fe/^{56}Fe$ ratio that can be estimated from the Bishunpur and Krymka troilite data of Tachibana & Huss (2003),[4] after the corrections of Telus et al. (2012; $1.32 (\pm 2.40) \times 10^{-8}$; $n = 32$; $\chi^2 = 0.44$). However, they are markedly different from the maximum $^{60}Fe/^{56}Fe$ ratios inferred from chondrule silicates (10^{-7}–10^{-6}; Figure 12) and from the average initial $^{60}Fe/^{56}Fe$ ratio of $9.2 (\pm 1.2) \times 10^{-7}$ calculated by Mostefaoui et al. (2005) for Semarkona troilites (Figure 12). The difference between our findings and those of Mostefaoui et al. (2005) remains significant ($>2\sigma$), even if we redo the linear regression of their troilite data following the method applied to our isotope ratios ($^{60}Fe/^{56}Fe = 9.53 (\pm 1.32) \times 10^{-7}$; $n = 19$; $\chi^2 = 1.06$), and even if we use only our Semarkona troilites for comparison (Table 3; $^{60}Fe/^{56}Fe = 1.75 (\pm 2.58) \times 10^{-7}$; $n = 11$; $\chi^2 = 1.09$).

There are several explanations for the discrepancy between the results of Mostefaoui et al. (2005) and our results. First, we consider the possibility that the nickel isotope compositions of our troilites were reset at some point during their history, e.g., by thermal metamorphism. Mostefaoui et al. (2005) emphasized that they did not analyze troilite that was in direct contact with metal because, as they argued, nickel might have diffused from troilite to metal upon heating on the parent body, which in turn would have negatively biased the calculated initial $^{60}Fe/^{56}Fe$ ratios. The meteorites studied here, including Semarkona, suffered very little, if any, thermal metamorphism (all are petrologic type 3.0–3.05; see Section 2). Their peak metamorphic temperatures were at or below 300°C–350°C (Alexander 1989; Huss et al. 2006), so element exchange between troilite and metal resulting from thermal metamorphism must have been limited. We did not find a systematic gradual increase in the nickel content of troilite toward nickel-rich metal in the sulfide-metal assemblages we later analyzed with NanoSIMS. Nevertheless, during our isotope analyses, we took care to set troilite measurement points at least $\sim 10\,\mu$m away from metal grains, if troilite was part of a metal-bearing mineral assemblage. We note, however, that most of the troilites we analyzed occurred in metal-free mineral assemblages. If we omit data of troilites from metal-bearing assemblages (Semarkona: b16-17, DOM 08006: b15, b16, and b47), the average inferred initial $^{60}Fe/^{56}Fe$ ratio remains indistinguishable from zero ($2.30 (\pm 2.08) \times 10^{-8}$; $n = 28$; $\chi^2 = 1.05$) and still significantly lower than that calculated by Mostefaoui et al. (2005). We therefore do not consider

[4] Bishunpur and Krymka are LL ordinary chondrites of petrologic types 3.15 and 3.2, respectively.

Table 3
Isotope Ratios of Chondritic Troilite Grains

Sample	Area of Interest	Troilite Textural Type[a]	Measurement	$^{56}Fe/^{62}Ni$[b]	±	$^{60}Ni/^{62}Ni$	±	$(^{46}Ti+^{46}Ca)/^{62}Ni$[c]	±	External Standard (Isotope Ratio)[d]	External Standard (Element Ratio)[d]	NanoSIMS Analysis Mode	Reg[f]
Semarkona	S5	ch	trox1	319464	7843	8.0595	0.4307	0.1185	0.0183	Sulfide	Sulfide	Image	*
		ch	trox2	293446	33226	7.2992	0.1736	0.0795	0.0065	Sulfide	Sulfide	Image	*
		ch	trox3	318285	35981	7.2493	0.1111	0.2381	0.0077	Sulfide	Sulfide	Image	*
	b14	ch	2-tro2	59804	555	7.1814	0.0711	0.1607	0.0040	NBS 446	NBS 446	Isotope	
	b16-17	ch	tro11	100746	1023	7.2518	0.0827	0.1529	0.0043	Sulfide	NBS 446[e]	Isotope	*
		ch	8-trox1	988383	109827	7.6567	0.4830	0.1837	0.0276	Sulfide	Sulfide	Image	*
		ch	8-trox2	538717	53659	7.4160	0.2603	0.0608	0.0083	Sulfide	Sulfide	Image	*
		ch	8-trox3	905251	164861	7.6266	0.4786	0.3498	0.0404	Sulfide	Sulfide	Image	*
		ch	8-trox4	353718	9603	7.3564	0.1087	0.1249	0.0052	Sulfide	Sulfide	Image	*
		ch	8-trox5	1259605	89183	6.6199	0.4754	0.0176	0.0089	Sulfide	Sulfide	Image	*
		ch	tro1	184448	1927	7.2431	0.0882	0.2755	0.0062	Sulfide	NBS 446[e]	Isotope	*
		ch	tro2	411128	11558	7.6840	0.2328	0.3594	0.0196	Sulfide	NBS 446[e]	Isotope	*
MET 00526	Ch3	ch	2-tro1	392103	46959	6.8023	0.2515	0.1274	0.0130	NBS 446	NBS 446	Image	
		ch	3-tro1	126904	15101	7.4045	0.1134	0.0787	0.0042	NBS 446	NBS 446	Image	
		ch	3-tro2	102872	12225	7.2787	0.1009	0.0217	0.0019	NBS 446	NBS 446	Image	
		ch	3-tro3	402488	15482	7.0446	0.2650	0.3727	0.0251	NBS 446	NBS 446	Image	
		ch	3-tro4	480170	20543	7.4557	0.3165	0.4738	0.0332	NBS 446	NBS 446	Image	
		ch	3-tro5	179920	20895	7.2661	0.1431	0.0332	0.0034	NBS 446	NBS 446	Image	
		ch	3-tro6	263752	12518	7.1825	0.1614	0.1310	0.0081	NBS 446	NBS 446	Image	
		ch	trox1	172079	20611	6.9323	0.2562	0.0569	0.0085	NBS 446	NBS 446	Image	
		ch	trox2	345346	41629	7.2157	0.2858	0.0867	0.0114	NBS 446	NBS 446	Image	
QUE 97008	b10	ch	trox1	76518	5579	7.3157	0.0957	0.1503	0.0051	NBS 446	NBS 446	Image	
		ch	trox2	52906	15205	7.1915	0.0918	0.1349	0.0044	NBS 446	NBS 446	Image	
		ch	trox3	68305	19646	7.3781	0.1290	0.2265	0.0084	NBS 446	NBS 446	Image	
DOM 08006	b1	rim	tro4	2715045	131165	7.5237	0.3832	0.2337	0.0251	Sulfide	Sulfide	Image	*
		rim	tro5	18279471	2427446	7.4564	1.0443	3.5263	0.5117	Sulfide	Sulfide	Image	*
	b2	m	trox1	9567040	818589	8.1152	0.7242	1.0657	0.1160	NBS 446	NBS 446	Isotope	
		m	trox2	8491339	667925	8.0892	0.6647	1.1809	0.1168	NBS 446	NBS 446	Isotope	
		m	trox3	12770642	1406280	7.2686	0.5833	0.3435	0.0473	NBS 446	NBS 446	Image	
	b3	m	tro2	2713589	439261	7.5047	0.2971	0.1239	0.0132	NBS 446	NBS 446	Isotope	
	b13	m	tro1_1	3685471	213586	7.4771	0.4591	10.3809	0.6269	NBS 446	NBS 446	Isotope	
		m	tro1_2	105792	2567	7.5891	0.1960	3.5902	0.0985	NBS 446	NBS 446	Isotope	
		m	tro2	12433611	1654420	8.0882	1.1219	1.3359	0.2270	NBS 446	NBS 446	Image	
		m	tro3_1	29497597	3022682	8.1022	0.8349	2.9472	0.3244	Sulfide	Sulfide	Isotope	*
		m	tro3_2	2060716	126187	7.4482	0.4319	0.1484	0.0223	Sulfide	Sulfide	Isotope	*
		m	tro3b	503070	26856	7.3401	0.2223	0.0618	0.0073	NBS 446	NBS 446	Image	
		m	tro3c	1257899	66073	7.3657	0.3800	0.1523	0.0203	NBS 446	NBS 446	Image	
		m	tro12	22349057	2486679	7.9274	0.9292	1.4570	0.2089	Sulfide	Sulfide	Image	*
		m	tro13_1	3804594	192335	7.5541	0.4041	3.0014	0.1726	NBS 446	NBS 446	Isotope	
		m	tro13_2	23643	212	7.2666	0.0695	0.1316	0.0035	NBS 446	NBS 446	Isotope	
	b15	rim	tro5	10323686	518060	7.0690	0.3628	72.4741	3.5159	Sulfide	Sulfide	Isotope	*
		rim	tro5b	14755900	1884162	7.8412	1.0591	2.1745	0.3345	Sulfide	Sulfide	Image	*
		rim	tro5c	1153385	57027	7.2054	0.3589	0.3083	0.0298	Sulfide	Sulfide	Image	*
		rim	tro14	8107042	359454	7.3458	0.3287	0.0514	0.0094	Sulfide	Sulfide	Isotope	*
	b16	m	tro1	5182461	259797	6.8089	0.3503	0.8161	0.0567	Sulfide	Sulfide	Isotope	*
		m	tro2	11686535	922927	7.4260	0.6083	0.9428	0.0983	Sulfide	Sulfide	Isotope	*
		m	tro4	6855139	1180329	6.4315	0.4780	0.4169	0.0507	NBS 446	NBS 446	Isotope	
		m	tro5	11565920	980853	8.1456	0.7152	0.5768	0.0736	Sulfide	Sulfide	Isotope	*
	b38	rim	tro2_1	743128	24685	7.6013	0.2686	0.0588	0.0082	NBS 446	NBS 446	Isotope	
		rim	tro2_2	133007	2123	7.3738	0.1255	0.0274	0.0027	NBS 446	NBS 446	Isotope	
		rim	trob1_1	82590	905	7.1017	0.0831	0.0389	0.0022	NBS 446	NBS 446	Isotope	
		rim	trob1_2	434282	11807	7.2785	0.2111	0.0391	0.0055	NBS 446	NBS 446	Isotope	
	b46	ch	trox1	8141368	742251	7.4438	0.6999	0.2904	0.0541	Sulfide	Sulfide	Image	*

Table 3
(Continued)

Sample	Area of Interest	Troilite Textural Type[a]	Measurement	$^{56}Fe/^{62}Ni$[b]	±	$^{60}Ni/^{62}Ni$	±	$(^{46}Ti+^{46}Ca)/^{62}Ni$[c]	±	External Standard (Isotope Ratio)[d]	External Standard (Element Ratio)[d]	NanoSIMS Analysis Mode	Reg[f]
		ch	trox2_1	11707012	1863179	7.3110	1.2226	0.5218	0.1401	Sulfide	Sulfide	Image	*
		ch	trox2_2	5273889	704026	5.3696	0.7651	0.1123	0.0465	Sulfide	Sulfide	Image	*
		ch	trox3	1994665	123735	7.4934	0.4640	0.0480	0.0131	Sulfide	Sulfide	Image	*
	b47	ch	trox1	818573	17345	7.3513	0.1783	0.1447	0.0087	Sulfide	Sulfide	Image	*
		ch	trox2	405554	8409	7.5872	0.1594	0.1516	0.0076	Sulfide	Sulfide	Image	*
ALHA77307	b1a	m	tro1b	3750078	327207	7.8251	0.5128	1.8279	0.1396	Sulfide	Sulfide	Image	*
		m	tro1c	2718682	329834	7.0800	0.7067	1.5271	0.1831	Sulfide	Sulfide	Image	*
		m	tro2b	3038311	378941	9.7468	1.1092	1.8549	0.2487	Sulfide	Sulfide	Image	*
		m	tro2c	4042482	453273	6.9556	0.6036	2.0292	0.2005	Sulfide	Sulfide	Image	*
	b1b	m	tro4	1520383	104142	7.2458	0.2309	0.1791	0.0136	Sulfide	Sulfide	Image	*
		m	tro5	2062235	158814	7.7089	0.3781	0.2073	0.0229	Sulfide	Sulfide	Image	*
	b2	m	tro1	1623717	141551	6.8008	0.2938	0.1077	0.0138	Sulfide	Sulfide	Image	*
		m	tro2	2162812	184295	7.5132	0.2870	0.1743	0.0161	Sulfide	Sulfide	Image	*
		m	tro3	1669729	139460	7.2497	0.2450	0.1394	0.0125	Sulfide	Sulfide	Image	*
		m	tro4	4235494	451179	8.1354	0.6313	0.3503	0.0498	Sulfide	Sulfide	Image	*
	b3	ch	tro1	1870472	92433	6.3255	0.3362	0.1538	0.0205	NBS 446	NBS 446	Isotope	
		ch	tro3	1900619	98392	7.6843	0.4075	0.4514	0.0006	NBS 446	NBS 446	Isotope	
		ch	tro4	1299236	60300	7.6461	0.3607	0.3378	0.0326	NBS 446	NBS 446	Isotope	
	b4	ch	tro1	377926	54735	7.1645	0.1626	0.0528	0.0049	NBS 446	NBS 446	Isotope	
		ch	trox2b	869836	113274	7.4513	0.2310	7.4513	0.2310	Sulfide	Sulfide	Image	*
		ch	trox3	580314	80671	7.3665	0.1901	7.3665	0.1901	Sulfide	Sulfide	Image	*
		ch	trox4	1108405	161095	6.8390	0.3575	6.8390	0.3575	Sulfide	Sulfide	Image	*
	b5	m	tro1	328642	51158	7.1178	0.1815	0.0579	0.0058	NBS 446	NBS 446	Isotope	
		m	tro2	454460	18388	7.3751	0.2093	0.0580	0.0065	NBS 446	NBS 446	Isotope	
		m	tro4_1	239294	37067	7.1705	0.1399	0.0569	0.0044	NBS 446	NBS 446	Isotope	
		m	tro4_2	200103	18288	7.2219	0.1167	0.0386	0.0030	NBS 446	NBS 446	Isotope	
		m	tro6	175457	27149	7.1964	0.1288	0.0182	0.0022	NBS 446	NBS 446	Isotope	
		m	tro6_2	151171	13770	7.2894	0.1027	0.0266	0.0021	NBS 446	NBS 446	Isotope	
	b7	rim	tro1	2394176	366972	7.0430	0.4069	0.1774	0.0230	NBS 446	NBS 446	Isotope	
		rim	tro3	1552922	232048	8.0798	0.3622	0.1829	0.0187	NBS 446	NBS 446	Isotope	
	b9	m	tro1	1398517	72802	7.1274	0.2891	0.1720	0.0169	Sulfide	Sulfide	Image	*
		m	tro2b	1677735	94416	6.9970	0.3260	0.1497	0.0179	Sulfide	Sulfide	Image	*
		m	tro3	2069098	124677	7.6230	0.3940	0.2085	0.0242	Sulfide	Sulfide	Image	*

Notes. NanoSIMS data.

[a] ch = chondrule, m = matrix, rim = sulfide occurring with iron-rich olivine in chondrule and CAI rims; see the Results section for details on classification.

[b] Calculated from measured $^{54}Fe/^{62}Ni$ ratios using sensitivity ratios estimated from measurements on the external standards and assuming a terrestrial $^{54}Fe/^{56}Fe$ ratio.

[c] Raw isotope ratios. ^{46}Ti and ^{46}Ca cannot be resolved from each other with NanoSIMS, hence the indication of both isotopes in the numerator.

[d] "Sulfide" indicates that a troilite with a low Fe/Ni ratio (<800; for normalization of $^{60}Ni/^{62}Ni$ ratios), or a nickel-rich sulfide (nickel content several weight percent or more; for the normalization of $^{56}Fe/^{62}Ni$ and $^{60}Ni/^{62}Ni$ ratios) within the same sulfide mass or association of sulfide ± metal was used for external normalization.

[e] Fe/Ni ratios estimated from NanoSIMS data for these analyses match Fe/Ni ratios obtained by EPMA within the uncertainty; therefore, we trust these Fe/Ni ratios, even though the NBS 446 steel was used for the external normalization of element ratios.

[f] Used for linear regression.

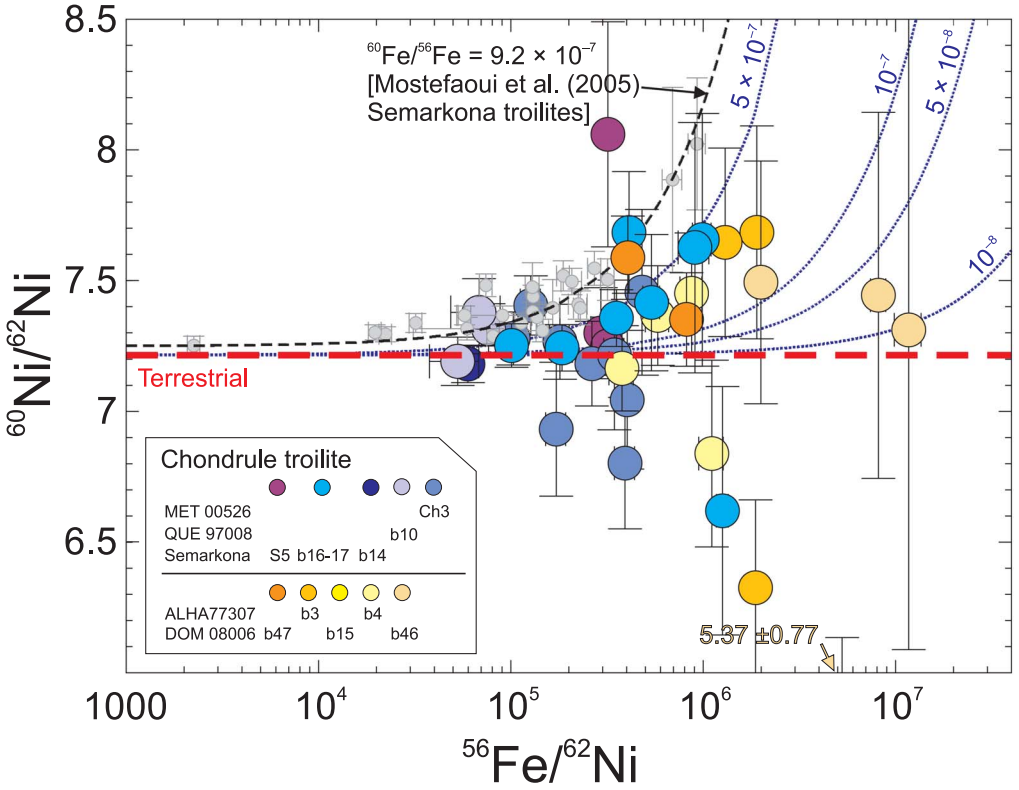

Figure 10. ^{56}Fe/^{62}Ni and ^{60}Ni/^{62}Ni ratios of chondrule troilites from the present study. ^{56}Fe/^{62}Ni ratios were calculated from ^{54}Fe/^{62}Ni ratios assuming terrestrial iron isotope ratios. Data for troilite grains from Semarkona (Mostefaoui et al. 2005; gray points), as well as (dotted blue) model curves indicating expected present-day isotope ratios for initial ^{60}Fe/^{56}Fe ratios from 10^{-8} to 5×10^{-7} (indicated in blue next to the curves) are displayed for reference. Error bars represent $\pm 1\sigma$.

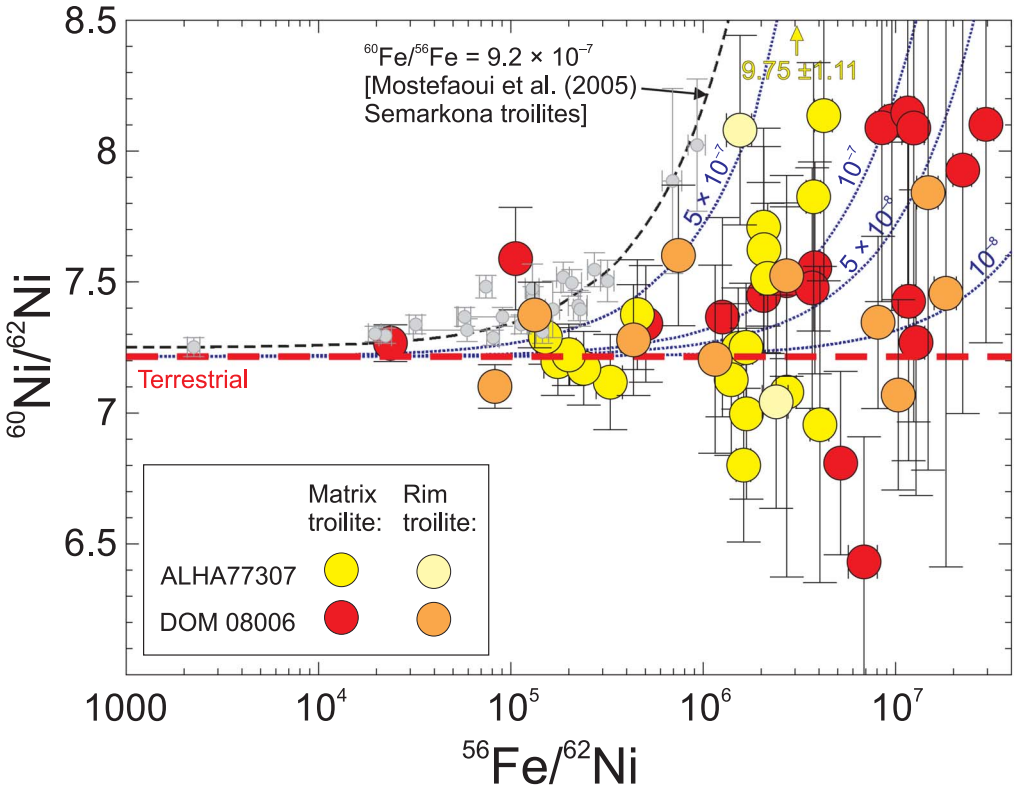

Figure 11. ^{56}Fe/^{62}Ni and ^{60}Ni/^{62}Ni ratios of rim and matrix troilites from the present study. ^{56}Fe/^{62}Ni ratios were calculated from ^{54}Fe/^{62}Ni ratios assuming terrestrial iron isotope ratios. Data for troilite grains from Semarkona (Mostefaoui et al. 2005, gray points), as well as (dotted blue) model curves indicating expected present-day isotope ratios for initial ^{60}Fe/^{56}Fe ratios from 10^{-8} to 5×10^{-7} (indicated in blue next to the curves) are displayed for reference. Error bars represent $\pm 1\sigma$.

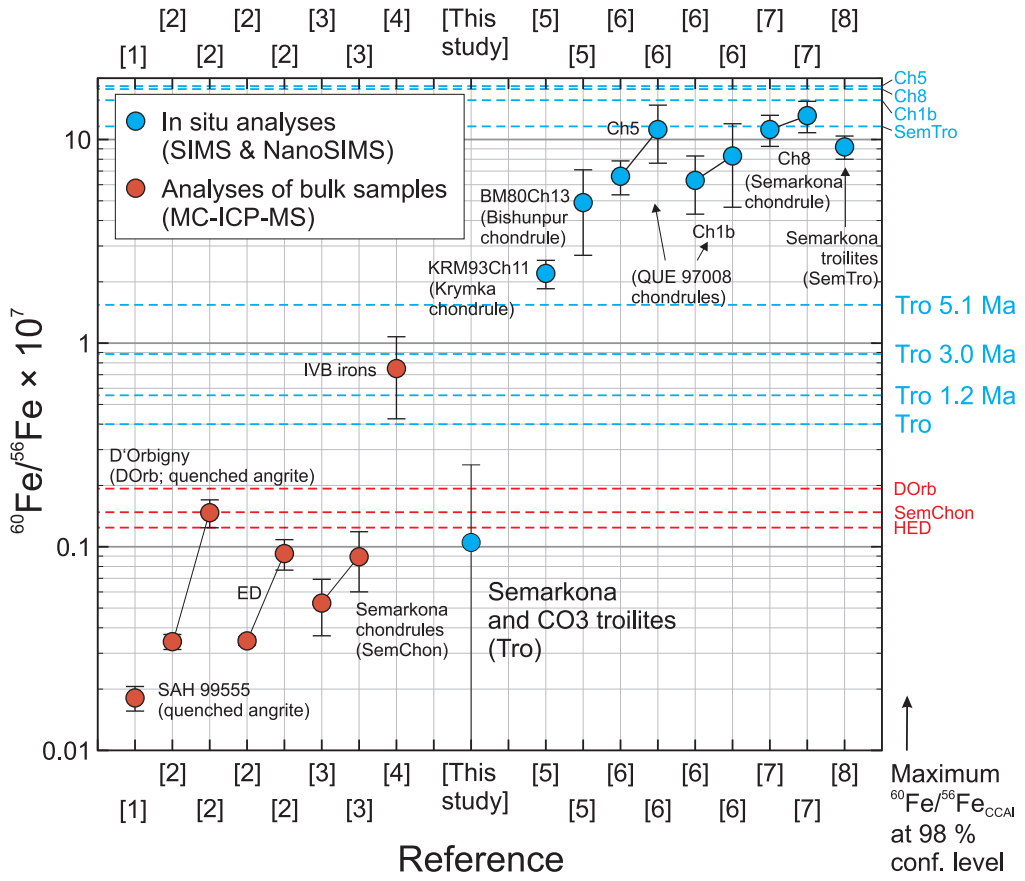

Figure 12. Inferred initial $^{60}Fe/^{56}Fe$ ratios of solar system objects as in Figure 1, but with additional data. Horizontal dashed lines are upper limits of initial $^{60}Fe/^{56}Fe$ ratios in different materials (indicated on the right) at the 98% confidence level, calculated from our own and literature data, using reported uncertainties. Upper limits of the $^{60}Fe/^{56}Fe$ ratio of the troilites studied here ("Tro") were calculated assuming different times of troilite formation after CCAIs (X Ma = X million years after CCAI formation; see Section 5.2 for age constraints).

metamorphic re-equilibration with metal in our samples to be a viable explanation for the lack of discernible nickel-60 from the in situ decay of iron-60.

Another explanation for the lower inferred initial $^{60}Fe/^{56}Fe$ ratios of our troilites could be that they are, on average, younger than the troilites analyzed by Mostefaoui et al. (2005). This, however, also seems unlikely. As shown above (Section 5.1), the troilites analyzed here probably formed by high-temperature nebular processes or through shock melting before the final assembly of their parent bodies. Thus, their formation time can be reasonably bracketed with chondrule formation and hydrothermal alteration on the parent body as upper and lower age limits, respectively. The age of Semarkona chondrules has been estimated from internal aluminum–magnesium isochrons by several authors. Based on the data of Kita et al. (2000), Rudraswami et al. (2008), and Villeneuve et al. (2009), Semarkona chondrules formed 1.24–3.00 million years after CCAIs. Chondrule ages are not available for ALHA77307 and DOM 08006, but age estimates exist for chondrules from the CO3.05 Yamato-81020 and the CO3-like, ungrouped Acfer 094 meteorites, again derived from internal aluminum–magnesium isochrons. According to these data, the chondrules' ages range from 1.66 (+0.165/−0.125) to 2.99 (+0.205/−0.145) million years after CCAI formation (Kurahashi et al. 2008; Ushikubo et al. 2010; Hertwig et al. 2019). Secondary phases related to aqueous alteration have not been dated directly in any of our samples, but the time of aqueous alteration on the L and CO parent bodies has been recently estimated using internal manganese–chromium isochrons obtained on fayalite from the Elephant Morraine 90161 (L3.05) and MacAlpine Hills 88107 (CO-like ungrouped type 3) chondrites (2.4 +0.9/−0.65 and 5.1 +0.25/−0.2 million years after CCAIs, respectively; Doyle et al. 2015). Mostefaoui et al. (2005) did not discuss in detail the processes that led to the formation of their troilites but suggested that their troilites could have formed coevally with chondrules. If we assume that the troilites analyzed by Mostefaoui et al. (2005) were all as old as the oldest Semarkona chondrules and that our troilites formed just before the aqueous alteration of the CO parent body, the maximum age difference between the troilites we analyzed and the troilites measured by Mostefaoui et al. (2005) is 3.87 ± 0.25 million years. During this time, the $^{60}Fe/^{56}Fe$ ratio inferred for the Semarkona troilites by Mostefaoui et al. (2005), $9.2 \pm 1.2 \times 10^{-7}$, should have dropped to $3.3 \pm 1.7 \times 10^{-7}$. This value is still much higher than the $^{60}Fe/^{56}Fe$ ratio inferred for our troilites ($1.05\ (\pm 1.48) \times 10^{-8}$), so an age difference cannot explain the discrepancy between our results and the results of Mostefaoui et al. (2005).

As mentioned in Section 1, nickel isotope data on bulk samples of differentiated early solar system bodies, especially on volcanic or subvolcanic rocks, in which the closure of the iron–nickel isotope system can be assumed to have occurred fast after formation (relative to the half-life of iron-60), are crucial to the evaluation of the accuracy of existing bulk and in situ nickel isotope data. Ancient volcanic rocks (i.e., old enough to incorporate live iron-60) with minimal alteration,

which come from the same isotope reservoir as UOC chondrules and troilites but represent thoroughly mixed material with nonchondritic Fe/Ni ratios, must provide fairly good estimates of the true $^{60}Fe/^{56}Fe$ ratio at their formation. This is because the Fe/Ni ratio of such rocks (e.g., quenched angrites, basaltic eucrites), or that of their constituent minerals cannot have changed enough through alteration or metamorphism, to cause an orders-of-magnitude downward shift in calculated $^{60}Fe/^{56}Fe$ ratios relative to the original values, while maintaining an isochron. For example, Tang & Dauphas (2012) estimated an initial $^{60}Fe/^{56}Fe$ ratio of $3.42 (\pm 0.29) \times 10^{-9}$ for the quenched angrite D'Orbigny, based on an internal mineral isochron ($n = 9$; $\chi^2 = 1.09$, intercept at the terrestrial $^{60}Ni/^{62}Ni$ ratio), which they obtained by analyzing bulk mineral and grain size separates. Given the age of D'Orbigny (4–5 million years after the formation of CCAIs; Schiller et al. 2010; Kleine et al. 2012; McKibbin et al. 2015), the $^{60}Fe/^{56}Fe$ ratio of D'Orbigny's precursors at solar system formation must have been between 1 and 1.3×10^{-8}, which is about two orders of magnitude lower than the highest $^{60}Fe/^{56}Fe$ ratios inferred from troilites and chondrule silicates by previous in situ studies (Figures 1 and 12). If we consider the previous in situ chondrule and troilite data to be accurate, it becomes difficult to explain how the Fe/Ni ratios of some D'Orbigny' minerals increased by orders of magnitude, while an isochron and its intercept at about the terrestrial $^{60}Ni/^{62}Ni$ ratio were maintained, and without destroying primary chemical zonation in the major constituents olivine and kirschsteinite (Mikouchi & McKay 2001; Floss et al. 2003). From this, it follows that in situ data suggesting orders-of-magnitude larger iron-60 abundance in UOC chondrules and troilites may not be accurate. Thus, a third explanation for the difference between the inferred initial $^{60}Fe/^{56}Fe$ ratios of our troilites and those of Mostefaoui et al. (2005) can be that the data set of Mostefaoui et al. (2005) suffers from some kind of analytical bias. One possibility is that the dynamic background correction they applied to the nickel isotopes was erroneous. This correction is specific for each mass, and for each analyte, and, for nickel, at the low count rates of our measurements, does not scale with the isotope's intensity, so its proportion to the actual isotope signal increases as the isotope signal intensity decreases. If the dynamic background of an isotope is not measured correctly, for example, because the measurement of the dynamic background is too short, a false isotope anomaly may result in the reduced data, with an amplitude that increases as the isotope's intensity decreases, thereby generating an "isochron."

5.3. Constraints on Iron-60 Abundance at Solar System Birth

Our in situ isotope data on chondritic troilites of high-temperature origin can be used to constrain the maximum abundance of ^{60}Fe in the early solar system. For this, we use the uncertainties of the inferred $^{60}Fe/^{56}Fe$ ratios of our troilites and the age constraints discussed in Section 5.2. Our estimates are displayed in Figure 12. Based on our troilite data, the initial $^{60}Fe/^{56}Fe$ of the solar system was less than 4.00×10^{-8}; at 98% confidence level, if we ignore the age of our troilites (horizontal dashed line in Figure 12, labeled "Tro"). If we assume our troilites formed about coevally with chondrules 1.2–3 million years after CCAIs (see Section 5.2), the initial $^{60}Fe/^{56}Fe$ of the solar system cannot have been higher than 5.55 to 8.85×10^{-8} (again, at the 98% confidence level; lines labeled "Tro 1 Ma" and "Tro 3 Ma," respectively, in Figure 12). Finally, if the troilites formed shortly before parent-body alteration is inferred to have occurred on the CO parent body (about 5 million years after CCAIs; see Section 5.2), the maximum initial $^{60}Fe/^{56}Fe$ of the solar system can be estimated at 1.54×10^{-7} (98% confidence level; line labeled "Tro 5.1 Ma" in Figure 12). As illustrated by Figure 12, these figures are much lower than the maximum $^{60}Fe/^{56}Fe$ ratios suggested by previous in situ work (e.g., Mostefaoui et al. 2005; Mishra et al. 2016), but higher than most of those calculated from the data of bulk samples (Figure 12).

6. Conclusion

We studied troilite in petrologic type 3 L and LL ordinary, as well as CO carbonaceous chondrites, with the ultimate goal of finding the signs of in situ iron-60 decay in them. We identified three texturally different troilites, for which a high-temperature magmatic origin could be inferred ("chondrule", "rim," and "matrix" troilite), based on micro- and nanopetrography (SEM, TEM), as well as mineral chemistry (EPMA, SEM-EDX, STEM-EDX).

In situ nickel isotope analysis of these troilites was conducted with the NanoSIMS, with higher spatial resolution than in previous SIMS/NanoSIMS studies. Our analyses did not indicate systematic enrichments in nickel-60, although the uncertainties of individual isotope measurements were large (up to 17%) due to the extremely low nickel contents of the studied troilites (atomic Fe/Ni ratios up to 1.17×10^6). We did not find any significant correlation between nickel-60 enrichments and Fe/Ni ratios, either in the entire set of troilite grains or in troilites of the same petrographic type (matrix, chondrule, chondrule rim). The average inferred initial $^{60}Fe/^{56}Fe$ ratio of the studied troilites (i.e., the $^{60}Fe/^{56}Fe$ ratio calculated for the entire troilite population) is $1.05 (\pm 1.48) \times 10^{-8}$. This value is very similar to those estimated in the past for Semarkona chondrules, angrites, as well as eucrites + diogenites, based on the isotope analyses of bulk samples (10^{-9}–10^{-8}; Figure 12), but about two orders of magnitude smaller than the average initial $^{60}Fe/^{56}Fe$ ratios inferred previously for Semarkona troilites and many chondrules from ordinary and carbonaceous chondrites (10^{-7}–10^{-6}; Figure 12) using in situ analysis techniques. Based on petrographic evidence and the generally unequilibrated nature of our samples, as well as on the timing of chondrule formation and planetary evolution, we conclude that the lack of discernible signs of in situ iron-60 decay in the studied troilites is not a result of metamorphic re-equilibration or the late formation of the troilites.

Although we cannot provide a definite explanation for the difference between the initial $^{60}Fe/^{56}Fe$ ratios inferred from in situ measurements and bulk analyses, our findings together with the recent in situ work of Trappitsch et al. (2018) on chondrule silicates strengthen the case that the high $^{60}Fe/^{56}Fe$ ratios estimated from in situ analytical data in the past were probably inaccurate.

We thank Elmar Gröner and Philipp Schuhmann for technical support on NanoSIMS. Our project was financially supported by the German Research Foundation (DFG) Special Priority Programme 1833 (grant Nos. HO2163/3-1, VO1816/4-1). Thin sections of QUE 97008, MET 00526, ALHA77307, and DOM 08006 were provided by the Antarctic Search for

Meteorites (ANSMET) program. US Antarctic meteorite samples are recovered by the ANSMET program, which has been funded by NSF and NASA, and characterized and curated by the Department of Mineral Sciences of the Smithsonian Institution and Astromaterials Curation Office at NASA Johnson Space Center. We also acknowledge funding of the ThermoFisher TEM "Themis" by the DFG via the Major Research Instrumentation Program under INST 211/719-1. The comments and suggestions of Andrew M. Davis and an anonymous reviewer helped greatly to improve the paper.

ORCID iDs

János Kodolányi https://orcid.org/0000-0001-5710-0537
Peter Hoppe https://orcid.org/0000-0003-3681-050X
Christian Vollmer https://orcid.org/0000-0002-7768-7651

References

Alexander, C. M. O'D., Barber, D., & Hutchison, R. 1989, GeCoA, 53, 3045
Alpert, S. P., Ebel, D. S., Weisberg, M. K., & Neiman, J. R. 2021, M&PS, 56, 311
Armstrong, J. T. 1991, in Electron Probe Quantitation, ed. K. F. J. Heinrich & D. E. Newbury (Boston, MA: Springer), 261
Birck, J. L., & Lugmair, G. W. 1988, E&PSL, 90, 131
Browne, E., & Tuli, J. K. 2013, NDS, 114, 1849
Castillo-Rogez, J., Johnson, T. V., Lee, M. H., et al. 2009, Icar, 204, 658
Cook, D. L., Meyer, B. S., & Schönbächler, M. 2021, ApJ, 917, 59
Davidson, J., Alexander, C. M. O'D., Stroud, R. M., Busemann, H., & Nittler, L. R. 2019, GeCoA, 265, 259
Diehl, R., Lugaro, M., Heger, A., et al. 2021, PASA, 38, e062
Dobrică, E., & Brearley, A. J. 2020, M&PS, 55, 649
Doyle, P. M., Jogo, K., Nagashima, K., et al. 2015, NatCo, 6, 7444
Dwarkadas, V. V., Dauphas, N., Meyer, B., Boyajian, P., & Bojazi, M. 2017, ApJ, 851, 147
Elliott, T., & Steele, R. C. J. 2017, RvMG, 82, 511
Floss, C., Crozaz, G., McKay, G., Mikouchi, T., & Killgore, M. 2003, GeCoA, 67, 4775
Floss, C., & Haenecour, P. 2016, LPICo, 1921, 6015
Gramlich, J. W., Machlan, L. A., Barnes, I. L., & Paulsen, P. J. 1989, J. Res. NIST, 94, 347
Grossman, J. N., & Brearley, A. J. 2005, M&PS, 40, 87
Guan, Y., Huss, G. R., & Leshin, L. A. 2007, GeCoA, 71, 4082
Hertwig, A. T., Kimura, M., Ushikubo, T., Defouilloy, C., & Kita, N. T. 2019, GeCoA, 253, 111
Hoppe, P., Cohen, S., & Meibom, A. 2013, Geostand. Geoanal. Res., 37, 111
Huss, G. R., Rubin, A. E., & Grossman, J. N. 2006, in Meteorites and the Early Solar System II, ed. D. S. Lauretta & H. Y. McSween (Tucson, AZ: Univ. Arizona Press), 567
Jacobsen, B., Yin, Q., Moynier, F., et al. 2008, E&PSL, 272, 353
Jogo, K., Nakamura, T., Noguchi, T., & Zolotov, M. Yu 2009, E&PSL, 287, 320
Kita, N. T., Nagahara, H., Togashi, S., & Morishita, Y. 2000, GeCoA, 64, 3913
Kleine, T., Hans, U., Irving, A. J., & Bourdon, B. 2012, GeCoA, 84, 186
Krot, A. N., Brearley, A. J., Petaev, M. I., et al. 2000, M&PS, 35, 1365
Kurahashi, E., Kita, N. T., Nagahara, H., & Morishita, Y. 2008, GeCoA, 72, 3865
Lauretta, D. S., & Buseck, P. R. 2003, M&PS, 38, 59
Lauretta, D. S., Lodders, K., & Fegley, B., Jr. 1997, Sci, 277, 358
Lauretta, D. S., Lodders, K., & Fegley, B., Jr. 1998, M&PS, 33, 821
Limongi, M., & Chieffi, A. 2006, ApJ, 647, 483
Mahon, K. I. 1996, IGRv, 38, 293
Marrocchi, Y., & Libourel, G. 2013, GeCoA, 119, 117
McKibbin, S. J., Ireland, T. R., Amelin, Y., & Holden, P. 2015, GeCoA, 157, 13
Mikouchi, T., & McKay, G. 2001, LPSC, 32, 1876
Mishra, R. K., & Chaussidon, M. 2014, E&PSL, 398, 90
Mishra, R. K., & Goswami, J. N. 2014, GeCoA, 132, 440
Mishra, R. K., Marhas, K. K., Sameer, et al. 2016, E&PSL, 436, 71
Moskovitz, N., & Gaidos, E. 2011, M&PS, 46, 903
Mostefaoui, S., Lugmair, G. W., & Hoppe, P. 2005, ApJ, 625, 271
Nanne, J. A. M., Nimmo, F., Cuzzi, J. N., & Kleine, T. 2019, E&PSL, 511, 44
Neumann, W., Kruijer, T. S., Breuer, D., & Kleine, T. 2018, JGRE, 123, 421
Nittler, L. R., Alexander, C. M. O'D., Davidson, J., et al. 2018, GeCoA, 226, 107
Norris, T. L., Gancarz, A. J., Rokop, D. J., & Thomas, K. W. 1983, JGR, 88, B331
Ostdiek, K. M., Anderson, T. S., Bauder, W. K., et al. 2017, PhRvC, 95, 055809
Quitté, G., Latkoczy, C., Schönbächler, M., Halliday, A. N., & Günther, D. 2011, GeCoA, 75, 7698
Quitté, G., Markowski, A., Latkoczy, C., Gabriel, A., & Pack, A. 2010, ApJ, 720, 1215
Rubin, A. E., Sailer, A. L., & Wasson, J. T. 1999, GeCoA, 63, 2281
Rudraswami, N. G., Goswami, J. N., Chattopadhyay, B., Sengupta, S. K., & Thapliyal, A. P. 2008, E&PSL, 274, 93
Rugel, G., Faestermann, T., Knie, K., et al. 2009, PhRvL, 103, 072502
Sahijpal, S., Soni, P., & Gupta, G. 2007, M&PS, 42, 1529
Schiller, M., Baker, J. A., & Bizzarro, M. 2010, GeCoA, 74, 4844
Schrader, D. L., Connolly, H. C., & Lauretta, D. S. 2008, GeCoA, 72, 6124
Schrader, D. L., & Lauretta, D. S. 2010, GeCoA, 74, 1719
Shukolyukov, A., & Lugmair, G. W. 1993, Sci, 259, 1138
Steele, R. C. J., Coath, C. D., Regelous, M., Russell, S., & Elliott, T. 2012, ApJ, 758, 59
Suttle, M. D., King, A. J., Ramkissoon, N. K., et al. 2022, GeCoA, 318, 83
Tachibana, S., & Huss, G. R. 2003, ApJ, 588, L41
Tang, H., & Dauphas, N. 2012, E&PSL, 359, 248
Tang, H., & Dauphas, N. 2015, ApJ, 802, 22
Telus, M., Huss, G. R., Nagashima, K., Ogliore, R. C., & Tachibana, S. 2018, GeCoA, 221, 342
Telus, M., Huss, G. R., Ogliore, R. C., et al. 2016, GeCoA, 178, 87
Telus, M., Huss, G. R., Ogliore, R. C., Nagashima, K., & Tachibana, S. 2012, M&PS, 47, 2013
Tomeoka, K., & Ohnishi, I. 2014, GeCoA, 137, 18
Trappitsch, R., Boehnke, P., Stephan, T., et al. 2018, ApJ, 857, L15
Ushikubo, T., Kimura, M., Nakashima, D., & Kita, N. T. 2010, LPSC, 41, 1491
Vescovi, D., Busso, M., Palmerini, S., et al. 2018, ApJ, 863, 115
Villeneuve, J., Chaussidon, M., & Libourel, G. 2009, Sci, 325, 985
Wallner, A., Bichler, M., Buczak, K., et al. 2015, PhRvL, 114, 041101
Warren, P. H. 2011, E&PSL, 311, 93
Wasserburg, G. J., Busso, M., Gallino, R., & Nollett, K. M. 2006, NuPhA, 777, 5
Yoshino, T., Walter, M. J., & Katsura, T. 2003, Natur, 422, 154
Zanda, B., Yu, Y., Bourot-Denise, M., & Hewins, R. 1997, Workshop on Parent-Body and Nebular Modification of Chondritic Materials, ed. M. E. Zolensky et al. (Houston, TX: Lunar and Planetary Institute), 68